

REPORT DOCUMENTATION PAGE

Form Approved OMB No. 0704-0188

Public reporting burden for this collection of information is estimated to average 1 hour per response, including the time for reviewing instructions, searching existing data sources, gathering and maintaining the data needed, and completing and reviewing the collection of information. Send comments regarding this burden estimate or any other aspect of this collection of information, including suggestions for reducing this burden to Washington Headquarters Services, Directorate for Information Operations and Reports, 1215 Jefferson Davis Highway, Suite 1204, Arlington, VA 22202-4302, and to the Office of Management and Budget, Paperwork Reduction Project (0704-0188), Washington, DC 20503.

1. AGENCY USE ONLY (Leave blank)		2. REPORT DATE 12 September 2002	3. REPORT TYPE AND DATES COVERED Final Report	
4. TITLE AND SUBTITLE Characterization of Fraglight Non-Woven Felt and Simulation of FSP's Impact in It			5. FUNDING NUMBERS N68171-01-M-5983	
6. AUTHOR(S) Sidney Chocron (Principal Investigator), A. Pintor, D. Cendon, C. Rosello, V. Sanchez-Galvez				
7. PERFORMING ORGANIZATION NAME(S) AND ADDRESS(ES) Fundacion Augustin de Betancourt, E.T.S.I. Caminos, Canales y Puertos, Universidad Politecnica de Madrid, Madrid 28040 - Spain				
9. SPONSORING/MONITORING AGENCY NAME(S) AND ADDRESS(ES) USARDSG-UK, Edison House 223 Old Marylebone Road, London NW1 5th			10. SPONSORING/MONITORING AGENCY REPORT NUMBER R&D 8927-AN-01	
11. SUPPLEMENTARY NOTES Final report for contract no. N68171-00-M-5983, 59 pages.				
12a. DISTRIBUTION/AVAILABILITY STATEMENT Approved for Public Release.			20021129 097 A	
ABSTRACT (Maximum 200 words) The non-woven felt known commercially as Dyneema Fraglight has an outstanding performances stopping fragments. The objective of this project is to understand the reason for this performance by means of four different approaches: 1) Through mechanical characterization varying size, direction, temperature and strain rate of specimens, 2) Ballistic characterization to obtain residual velocity curves and high speed photography, 3) Numerical simulations of static and ballistic tests, 4) Analytical modeling. All the approaches were covered, although the analytical work would need more work to complete. The mechanical characterization has shown that the felt is orthotropic, very size dependent, that it weakens appreciably at 100 C and up to strain rates of $10^3 s^{-1}$ its properties do not suffer a large modification. The ballistic tests show that the felt is actually better than what the manufacturer claims (with the boundary conditions used in this project). The numerical simulations confirm that the huge deformation suffered by the felt during the ballistic impact is the key for its outstanding performance. An analytical simulation of a non-homogenous, non-linear and under very high strains is extremely difficult from first principles, though a constitutive equation for an elastic, orthotropic fibrous material, with arbitrary distribution of fibers has been developed.				
14. SUBJECT TERMS US Army Research, Spain, Polyethylene, Non-woven felt, Mechanical characterization, Body armor, High strain rate, Dyneema Fraglight, Fabric target, Numerical simulation of impact in textiles			15. NUMBER OF PAGES	
			16. PRICE CODE	
17. SECURITY CLASSIFICATION OF REPORT Unclassified	18. SECURITY CLASSIFICATION OF THIS PAGE Unclassified	19. SECURITY CLASSIFICATION OF ABSTRACT Unclassified	20. LIMITATION OF ABSTRACT Unlimited	

NSN 7540-01-280-5500

Standard Form 298 (Rev. 2-89)
Prescribed by ANSI Std. Z39-18
298-102

**Characterization of Fraglight Non-Woven Felt and
Simulation of FSP's Impact in It**

5927ANO1

Sidney Chocron
(Principal Investigator)

Francisco Gálvez

A. Pintor

D. Cendón

C. Roselló

V. Sánchez-Gálvez

Prepared for
United States Army
European Research Office of the U.S. Army
London, England

Contract no.: N68171-00-M-5983

Contractor:
Fundación Agustín de Betancourt
E.T.S.I. Caminos Canales y Puertos
Universidad Politécnica de Madrid
Madrid 28040 - SPAIN

DISTRIBUTION STATEMENT A
Approved for Public Release
Distribution Unlimited

Final Report

The Research reported in this document has been made possible through the support and sponsorship of the U.S. Government through its European Research Office of the US Army. This report is intended only for the internal management use of the Contractor and U.S. Government

AQ F03-01-0200

Table of Contents

1	Introduction	6
2	Material Characterization.....	7
2.1	Introduction	7
2.2	Mechanical Testing.....	8
2.2.1	Tensile testing of single fibers	8
2.2.2	Search of a characteristic length of the fiber.	10
2.2.3	Dependence of properties on the direction of application of load	14
2.2.4	Dependence of properties on temperature	16
2.2.5	Stress-strain curves at medium strain rates.....	18
2.2.6	Hopkinson Bar Testing.....	19
2.2.7	Out-of-Plane Testing	25
2.2.8	Summary.....	30
2.3	Ballistic Testing	31
2.3.1	Introduction.....	31
2.3.2	Test Procedure.....	34
2.3.3	Results for the 17-grain FSP	35
2.3.4	Results for the 4-grain FSP	36
2.3.5	High Speed Imaging of the back of the target.	38
2.3.6	Discussion and Summary	40
3	Numerical Simulations.....	40
3.1	Introduction	40
3.2	Numerical Simulations of static tensile tests with ABAQUS	43
3.3	Numerical Simulations of the impact of FSPs with Autodyn 3D.....	44
3.4	Numerical Simulations of the impact of FSPs with Autodyn 2D.....	48
3.5	Numerical Simulations of FSPS impact with LS-DYNA	50
3.6	Summary and Conclusions	51
4	Analytical Simulations.....	51
4.1	Bibliographic search and possibilities of exploitation	53
4.2	Constitutive equation	58
4.3	Summary	

Table of Figures

Figure 1: Definition of transverse and longitudinal direction in the roll of Fraglight	7
Figure 2: Load-strain curve for a single fiber of Dyneema SK75	8
Figure 3: Two micrographs of a single fiber of Dyneema SK 75.....	9
Figure 4: Tensile test setup with LVDT device to measure the strain.	10
Figure 5: Summary of the size effect tensile tests.....	11
Figure 6: 1/4 th Scaled pictures of a test. The specimen 100 mm x 100 mm.....	12
Figure 7: Dependence of the stress-strain curve with direction of application of load ...	14
Figure 8: a) 45-degrees specimen, b) 90-degrees specimen	15
Figure 9: a) Specimen and b) high temperature test set up.....	16
Figure 10: Temperature study on Dyneema Fraglight	17
Figure 11: Strain rate dependence of stress-strain curve	18
Figure 12: The Hopkinson bar of the laboratory.....	19
Figure 13: Amplifier, oscilloscope and computer used in the Hopkinson bar tests.....	20
Figure 14: A specimen mounted in the Hopkinson bar before the test.....	21
Figure 15: Diagram of the Hopkinson bar specimen.	21
Figure 16: Comparison of the results obtained in the Hopkinson bar and in the static tests	22
Figure 17: A specimen after the Hopkinson bar test.	22
Figure 18: Measuring the sound velocity in the felt with the Hopkinson bar	23
Figure 19: Sound velocity as a function of the pre-strain.....	24
Figure 20: Diagram of an Out of Plane test	25
Figure 21: Set-up of Out of Plane tests.....	26
Figure 22: Close view of tup and clamps	26
Figure 23: Size effect in the out of plane testing (5 mm/min).....	27
Figure 24: Size effect in the out of plane testing with drop weight machine (3.6 m/s) ..	27
Figure 25: The Drop Weight Tester and the specimen mounted inside it.....	28
Figure 26: Strain rate effect in a 20 mm diameter specimen	29
Figure 27: Strain rate effect in a 40 mm diameter specimen.	29
Figure 28: Strain rate effect in the 60 mm diameter specimen.....	29
Figure 29: a) A specimen before and after being tested with the 20 mm diameter clamp.	
b) A close view of a specimen tested with the 60 mm clamp.	30
Figure 30: Set-up of the shooting tests.	31
Figure 31: Photography and drawing of the circuit used to measure the residual velocity	32
Figure 32: Wooden frame and residual velocity measurement device.....	33
Figure 33: Set-up of the four CCD cameras and mirror used to track the back of the target with high-speed photography.	33
Figure 34: Residual velocity vs. Striking velocity for the 17-grain FSP impacting normally 1 to 3 layers of non-woven Dyneema	34
Figure 35: Residual velocity vs. striking velocity for normal and 45° impact of the 17 grain FSP into three layers of non-woven Dyneema.	35
Figure 36: Residual velocity vs. striking velocity of the 4-grain FSP for 1,2 and 3 layers of Fraglight.....	36
Figure 37: Photographs at 0, 40 μ s, 90 μ s and 290 μ s. Striking velocity 361 m/s. One layer	37
Figure 38: Photographs at 0, 45 μ s, 95 μ s and 235 μ s. Striking velocity 524 m/s. Two layers.....	38

Figure 39: Two possibilities in an oblique impact into a unidirectional layer: a) velocity contained in the plane perpendicular to the fibers, b) velocity contained in the plane of the fiber.	39
Figure 40: Load per Length vs. True Strain Curves for three different directions. Thin lines are the real tests while thick lines are the predictions calculated with ABAQUS.	41
Figure 41: Strains calculated with the ABAQUS in tensile static tests: a) Transverse, b) 45 deg., c) Longitudinal	42
Figure 42: Photographs of the deformed shape during real tests: a) Transverse, b) 45 deg., c) Longitudinal	42
Figure 43: Determination of the material parameters that could possibly reproduce the impact. All the calculations are for the 17-grain FSP against one layer of Fraglight	45
Figure 44: Residual velocity vs. striking velocity for the 17 grain FSP projectile. The curves fit the experimental results, the triangles, squares and circles are the AUTODYN predictions.	46
Figure 45: : Residual velocity vs. striking velocity for the 4-grain FSP projectile. The curves fit the experimental results, the triangles, crosses and circles are the AUTODYN predictions.	47
Figure 46: Example of a Yield strength model dependent on the strain rate.....	47
Figure 47: Results with a Yield strength strain rate dependent.	48
Figure 48: Shell mesh used in the LS-DYNA calculations.	49
Figure 49: Sequence of the impact of 17 grain FSP into 1 layer of Fraglight seen from the back.	49
Figure 50: Comparison of Chocron analytical results and FSP experiments in the non-woven felt.	52
Figure 51: Comparison of Walker model results and experimental ballistic limits.....	52
Figure 52: Reference and deformed configuration	53
Figure 53: Principal strains orthonormal base	56

1 Introduction

The non-woven felt known commercially as Dyneema Fraglight has an outstanding performance stopping fragments. The manufacturer claims that a stack with an areal density of 1.2 kg/m^2 can stop a 17 grain (1.1 gram) fragment simulating projectile at 450 m/s. The objective of this project is to understand the reason for this performance by means of four different approaches:

- 1) Thorough mechanical characterization where tensile tests were performed varying the size from 1 mm to 150 mm, the direction of load (0, 45 and 90 degrees), the temperature from 20C to 100C and the strain rate of tensile tests from 10^{-3} s^{-1} to 10^3 s^{-1} . Out-of-plane punching tests were also performed with different sizes and velocities of application of load.
- 2) Ballistic testing of 1 to 3 layers at normal and oblique impact. Two different projectiles were used, 4-grain FSP and 17-grain FSP. High speed photography was used to track the deformation of the back of the target
- 3) Numerical simulation of static and ballistic tests. The numerical simulation of the static tensile tests was performed with the finite element code ABAQUS. The tests simulated were specimens of 100 mm x 100mm size and in three different directions of load. The ballistic tests were simulated using the 2-D and 3-D versions of AUTODYN as well as LS-DYNA.
- 4) The analytical modeling consists only of the mathematical apparatus needed to find a constitutive equation for a fibrous orthotropic material, but with the limitations of linear elasticity, that, given the results of the characterization, might be very far from reality.

The results obtained in parts 1 through 3 have been presented as oral papers in the ARA annual meeting in Canada, 2001, and in the International Ballistic Symposium in Orlando, in 2002, as well as published in their respective proceedings.

2 Material Characterization

2.1 Introduction

The Dyneema Fraglight was delivered as a 100 m long roll its width being 1.6 m. The width will be called the transverse direction of the roll in this report, while the length will be called the longitudinal direction, see Figure 1.

To the author's knowledge there is no work available in the literature with properties of this material, although there are a lot of works in other non-woven felts or woven fabrics.

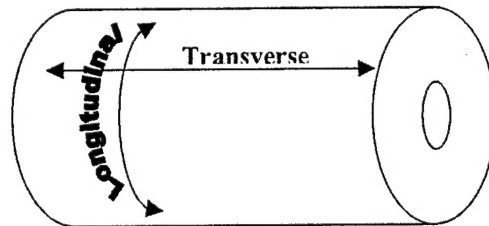


Figure 1: Definition of transverse and longitudinal direction in the roll of Fraglight

This chapter explains in detail all the experiments performed as well as the results and conclusions gathered from them. It begins with microscopic observation of the fiber and tensile testing of a single fiber, to follow with standard tensile tests of the whole felt for different sizes, directions of load, temperature and strain rates. Out of plane tests are also presented. To finish the chapter the ballistics tests are described and residual velocity curves plot. The high-speed photography allowed tracking the longitudinal and deflection (transverse) waves. Without counting the ballistic tests, the number of mechanical tests performed is over 150.

2.2 Mechanical Testing

2.2.1 Tensile testing of single fibers

Introduction

Although the tensile testing of single fibers was not the objective of this project, a few tests were carried out to confirm the properties of the fiber given by the manufacturer. Together with the non-woven felt roll a bobbin with a single yarn (a few meters long), identical to the one used in the felt, was requested and some tests performed. The fiber was observed in the electronic microscope and its diameter estimated.

Procedure

The tensile testing machine for the single fibers was a small INSTRON machine with a maximum load of 5 kN. The load was measured with a weighing machine that had a resolution of 1 centigram. The fiber was glued to a paper frame that surrounded it. The paper frame was attached to an aluminum frame that rested on the weighing scale. Before the test the paper frame was cut and the fiber loaded in tension from the top forcing the fiber to try to lift the dead weight of the aluminum, and consequently stretching and unloading the weighing scale. The loss of load in the scale is equal to the load on the fiber. The strain in the fiber was measured through the displacement of the actuator of the testing machine.

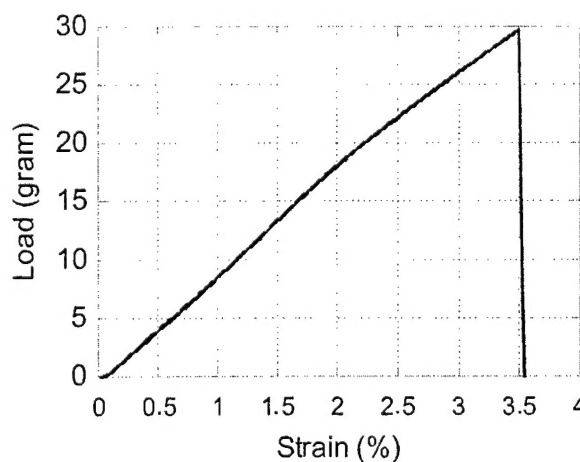


Figure 2: Load-strain curve for a single fiber of Dyneema SK75

Results

A total of four tests were performed on single fibers, but only three were valid (the fiber slipped in one of them). Figure 2 is the typical load-strain curve obtained. From the micrographs (Figure 3) the diameter of the fiber was estimated to be 8 μm , so the Young modulus measured is 170.5 GPa, the strain to failure 3.5% and the fibers is elastic up to failure. These results published by DSM are 110 GPa, 3.6 % strain to failure. In two of the tests the fibers were actually unloaded and reloaded without showing any permanent deformation. The discrepancy in the Young modulus probably comes from an underestimation of the fiber diameter, which is not provided by the manufacturer.

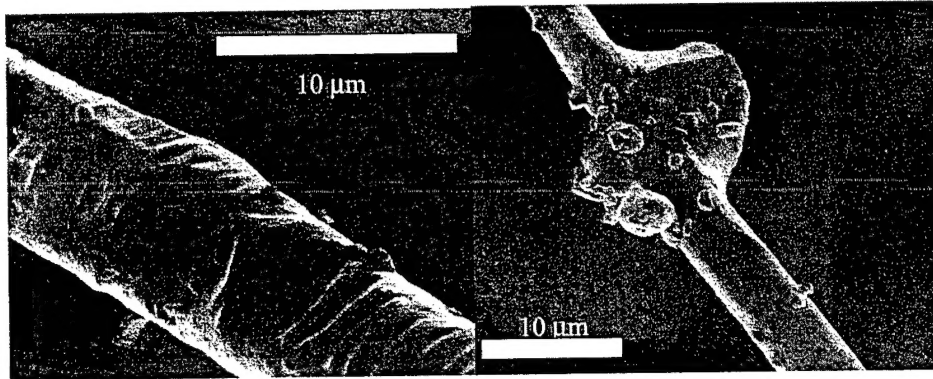


Figure 3: Two micrographs of a single fiber of Dyneema SK 75

Analysis

From Figure 2 it can be concluded that Polyethylene single fibers behave elastically and are brittle. The micrographs show that the fibers have sometimes some defects like "wrinkles" or bulges.

2.2.2 Search of a characteristic length of the fiber.

Introduction

The Fraglight is a non-woven felt made of short fibers. This microstructure is the origin of a strong dependence of the properties on the size of the specimen tested. The authors think it is interesting to study this size effect that should be taken into account when dealing with analytical or numerical models of the material in the second part of this project.

Procedure

All the tensile tests in the non-woven felt were performed in an INSTRON 8501 testing machine with a maximum load of 100 Ton and a maximum actuator speed of 500 mm/min. The load during the tests was measured with a 25 kN INSTRON load cell. The loading process was slow, around 10^{-3} s^{-1} of strain rate. The strain was measured in three different ways that were compared to confirm the results were reliable:

- 1) The strain was measured with the displacement of the actuator, dividing its displacement by the initial length of the specimen.
- 2) An INSTRON LVDT device checked that the actuator displacement given by the console was accurate enough. Figure 4 shows a 30 mm long specimen (test #107), the gripping system, the actuator and the LVDT device.

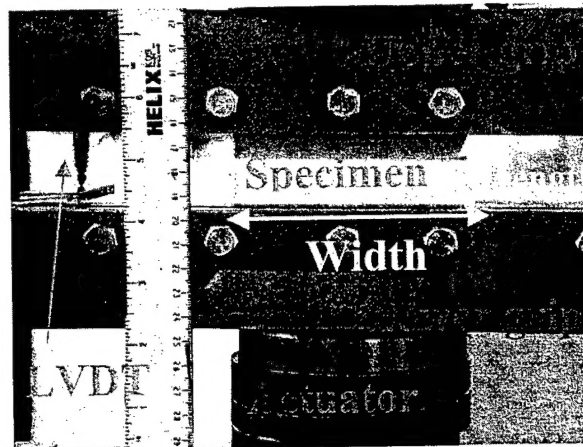


Figure 4: Tensile test setup with LVDT device to measure the strain.

- 3) Many tests were recorded in 8 mm videotape, with a digital camera, using special software capable of tracking with a mouse the strain between two marks in the specimen (being) tested. Again the strain values obtained were similar to those measured with either the actuator displacement or with the LVDT.

It is important to point out that the specimens were cut from the roll with a well-sharpened knife. It is much easier to cut the specimens with hot scissors than to melt the borders, but it was observed that the strength increased dramatically. In fact, melting the borders is equivalent to hold its fibers in place without allowing slipping between one another, hence stiffening and strengthening the specimen.

Results

The tests performed consisted in tensile tests of specimens where the length was ranging (varied) from 10 to 100 mm, while the width was kept constant (100 mm). The specimens were always tested in the transverse configuration, meaning that its length direction was transverse to the roll where the specimen was cut from.

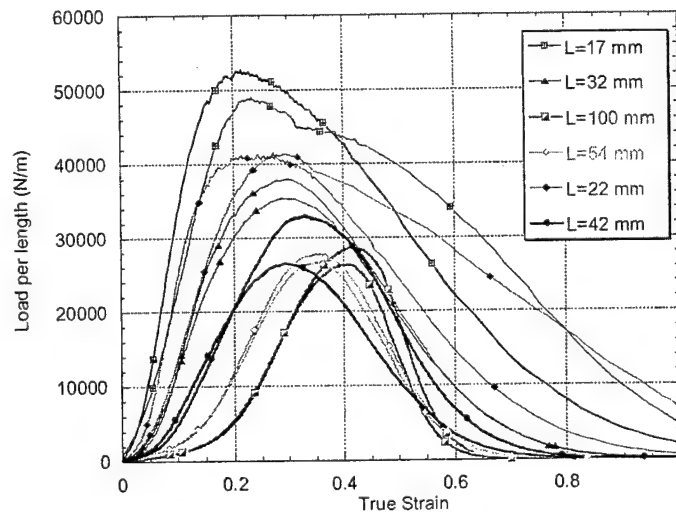


Figure 5: Summary of the size effect tensile tests

Specimens of nominal lengths of 10, 20, 30, 40, 50, 60 and 100 mm were tested obtaining the results plotted in Figure 5. At least three tests per specimen were performed, although not all of them are shown in the figure. As it was expected short specimens are much stronger and stiffer than long specimens, but those longer than 40 mm have similar properties. The authors do not think that the specimens of 100 mm

length have a higher strain to failure, but rather that there is a two dimensional effect since the specimen's width decreases remarkably during the test much more in long than in short specimens. Note that all the loads are given per unit of length, i.e. the load measured during the test was divided by the width of the specimen. These units (N/m) are usually used in the context of fabrics since it is not possible to measure their thickness. An "effective" thickness might be defined as the areal density divided by the volumetric density, as it will be used in the future to calculate stresses.

Analysis

There is an important size effect with Dynecma Fraglight. According to the manufacturer the process to obtain the non-woven felt is to cut short fibers of around 5 cm, comb and stack them in several layers, and finally needle punched the layers. The tensile tests indeed show that above 4 or 5 cm its behavior changes and its strength reaches a minimum.

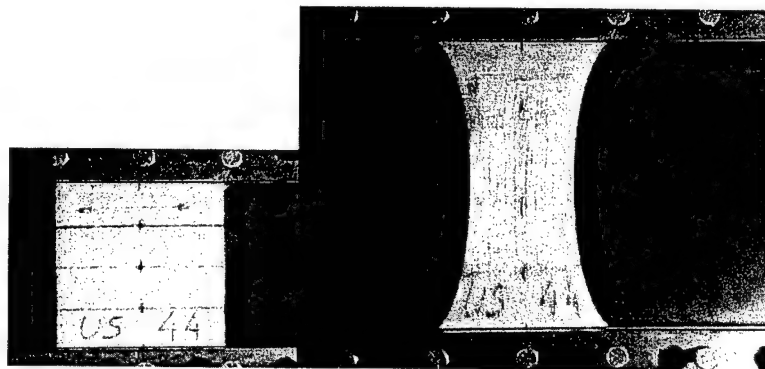


Figure 6: 1/4th Scaled pictures of a test. The specimen 100 mm x 100 mm

Figure 6 is a scaled photography of test #44. The load was applied in the transverse direction of the roll and the specimen was 100 mm x 100 mm size. The Poisson effect is remarkable, but clearly the test is far from being uniaxial: the strain in the transverse direction of the load is zero in the grips and around 40% in the center of the specimen. A rough estimation (because the test is not uniaxial) could be 0.4, however a better estimation will be obtained later with the help of a numerical simulation of this test.

The stiffness also depends on the size of the specimen. Short specimens are stiffer and more linear than long specimens. All the specimens show a softening part after failure.

It seems reasonable, from the load curves, to assume that the first part of the curve corresponds to the alignment and disentanglement of the fibers. Once they are aligned the felt behaves almost elastically up to failure. The failure is progressive following a smooth curve that probably corresponds to a progressive break-up of more and more fibers and ensuing slipping

2.2.3 Dependence of properties on the direction of application of load

Introduction

Anisotropy is an important factor to be taken into account in the modeling of materials. In fact anisotropy should be avoided in ballistic applications since it implies a “weak” direction, the one where the sound speed is lower. If the strain does not propagate fast through the fabric, it concentrates under the projectile, triggering an early failure of the fabric. This effect should be considered in the numerical models, and means that a three-dimensional code might be needed to obtain a reasonable result. The manufacturing process of Dyneema described above involves the step of fibers brushing. As it will be shown this brushing process is, potentially, the source of an important anisotropy in this material. The test procedure is identical to that described in 2.2.2., so it will not be explained in detail again.

Results

Figure 7 shows the stress-strain curves for three different directions. 0 degrees means the load was applied in the transverse direction of the roll, 90 degrees is the direction of the roll.

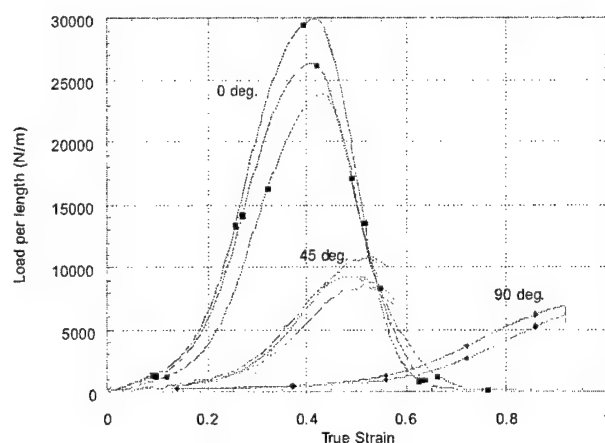


Figure 7: Dependence of the stress-strain curve with direction of application of load

The transverse direction of the roll is not only 3 or 4 times stronger than the longitudinal, but also much stiffer. In fact the specimens (which were 100 mm x 100

mm) could not be broken in the 90 degrees specimens because the INSTRON machine reached its maximum stroke (150 mm). The 45 degrees specimens behaved in between. Figure 8 a) is a picture of a 45 degrees specimen failing in shear, b) is a longitudinal specimen. The reader can appreciate the high strain to failure of this specimen, which was at the beginning of the test a square 100 mm x 100 mm. The engineering strain to failure is more 150%, while the true strain is around 80%

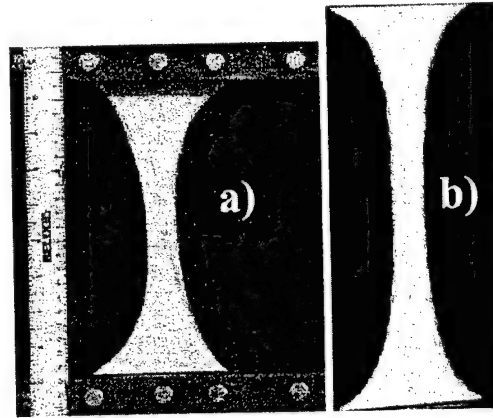


Figure 8: a) 45-degrees specimen, b) 90-degrees specimen

Analysis

Although it is impossible to see whether there is a preferred direction for the fibers, because at sight they look randomly distributed, from the test curves it is reasonable to assume that most of the fibers are aligned with the direction transverse to the roll. When the specimen size is smaller than the fiber length, for instance 20 mm as in Figure 5, many fibers are clamped at both ends and the felt behavior is almost linear until failure. It will also be shown with the high-speed photography that the sound speed in the 0 degrees direction is larger than in the orthogonal. For ballistic applications, if stacking is needed it should be done with a 0/90 stacking sequence to obtain a balanced target.

2.2.4 Dependence of properties on temperature

Introduction

Polyethylene is known to be very sensitive to temperature, which is one of its potential disadvantages when used for ballistic protection in vehicles. Inside a vehicle the temperature in a sunny day can easily reach 80 C, and the hull might be even warmer. Besides, the felt is supposed to stop fragments coming from explosions, which will also probably be at high temperature. These facts easily justify a characterization of the felt at high temperatures, where “high” in this material is a temperature of only 100 C.

Procedure

The specimens were placed inside an INSTRON climatic chamber that can reach 600 C. The temperature was monitored with a gage as shown in Figure 9. Part b) of the figure shows the whole setup during the test. On the left of the testing machine is the temperature display, on the right the electronics console. The computer used to control the machine and record the data does not appear in this image. All the specimens were kept at the temperature of the test during 30 minutes prior to the beginning of the tensile test. Specimens of size 100 mm x 100 mm (also some 50 mm x 100 mm) were tested at room temperature (20 C), 50 C and 100 C.

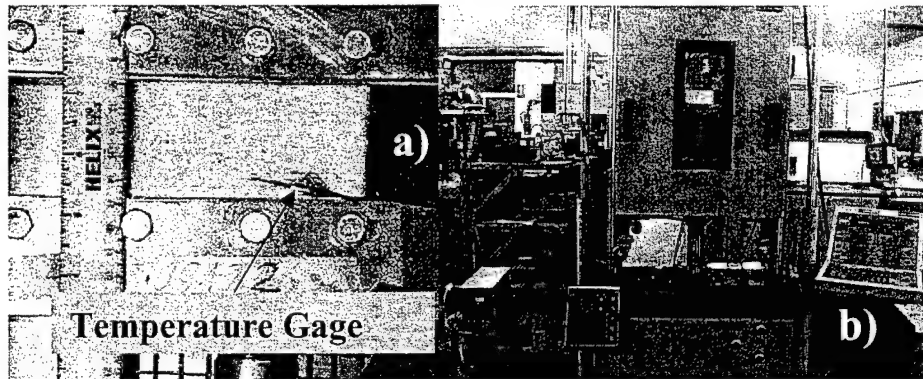


Figure 9: a) Specimen and b) high temperature test set up.

Results

Figure 10 clearly demonstrates that the felt is weakened (20 %) at moderate temperatures (50C). At 100C both the strength and the strain to failure decrease

significantly: the strength by 40% and the strain by 60%. This would probably mean that the performance at high temperature of Fraglight armor is very poor.

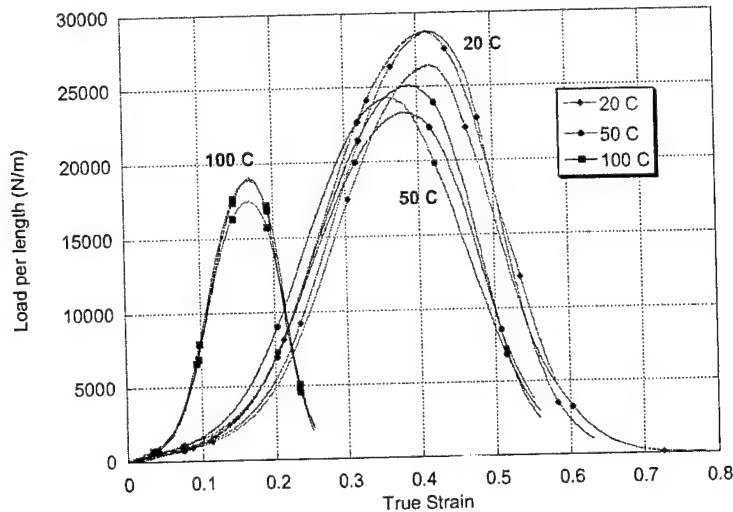


Figure 10: Temperature study on Dyneema Fraglight

Analysis

Dyneema Fraglight is made of polyethylene fibers, so the temperature was expected to weaken considerably the felt. Temperature should be another factor to be taken into account when modeling impact on Fraglight, since probably some melting of the fiber takes place during projectile penetration. It is remarkable to observe that actually the felt is stiffer at high temperature. Possibly some bonding between the fibers was beginning to happen not allowing them to slip and untangle.

2.2.5 Stress-strain curves at medium strain rates

Introduction

The structure of the felt, with short fibers entangled, seems to anticipate a strong dependence of the properties with strain rate. At high velocity the fibers should not have time to disentangle when strained and hence the felt would appear stiffer than at low velocities. This strain rate dependence might be very important when trying to simulate numerically or analytically the penetration process.

Tests were performed at strain rates ranging from 10^{-3} s^{-1} to 10^3 s^{-1} . The range of 10^{-3} s^{-1} to 1 s^{-1} was covered with the INSTRON testing machine, while the tests at high velocity (10^3 s^{-1}) were performed with the Hopkinson bar.

Results of medium strain rate tests

Specimens of size 50 mm x 50 mm were tested in tension, at three different velocities: 10^{-3} s^{-1} , 10^{-2} s^{-1} and 1 s^{-1} . The results are shown in Figure 11. Each curve in that figure is the average of three curves obtained in three different experiments. All the tests were carried out with the same gripping system. No difference is evident in the behavior of the felt at low and medium velocities.

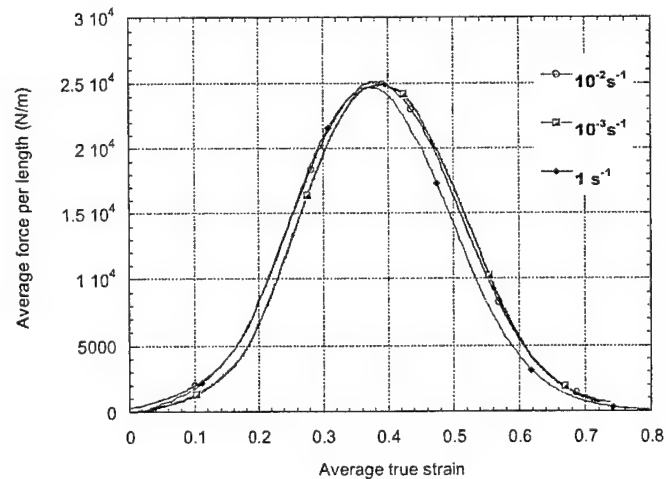


Figure 11: Strain rate dependence of stress-strain curve

2.2.6 Hopkinson Bar Testing

Test Description

The Hopkinson bar tests are tensile tests at high strain rate (1000 s^{-1}). The specimen is attached with special grips on one end to the incident (or input) bar and on the other end to the output bar. Figure 12 displays all those elements. A long projectile launched with a compressed air gun pulls the incident bar creating a one-dimensional tensile pulse that travels until it reaches the specimen. The pulse is registered by strain gages glued to the bars. The pulse pulls the specimen at around 20 m/s, stretching and breaking it. Part of the pulse is transmitted to the output bar; in fact the signal received by the output bar is proportional to the load sustained by the specimen.

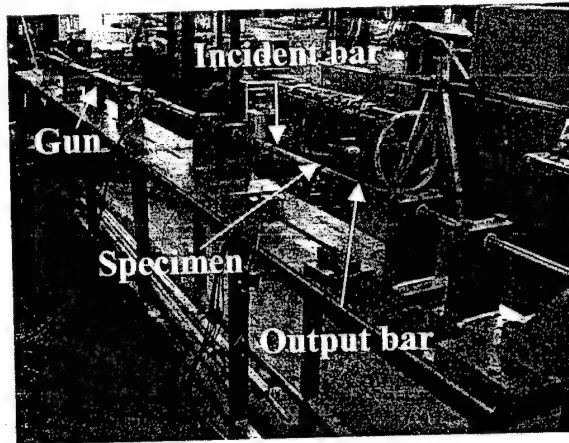


Figure 12: The Hopkinson bar of the laboratory

The output bar shown in the photograph is a 22-mm diameter steel bar of very high elastic limit that was not sensitive enough to the low loads supported by the specimen. A new aluminum bar with a smaller diameter (10 mm) was designed to gain accuracy during the tests. The aluminum has a lower elastic modulus, almost a third that of the steel, and the section is less than a fourth, hence we amplify the waves or the strain seen by the strain gages a factor of $4 \times 3 = 12$.

The strain gages are part of a Wheatstone bridge (in these experiments $\frac{1}{4}$ of a bridge) that is completed inside an amplifier. The amplifier casts its signal to a Tektronix oscilloscope that registers the waves at three different points, two in the incident bar and one in the output bar.

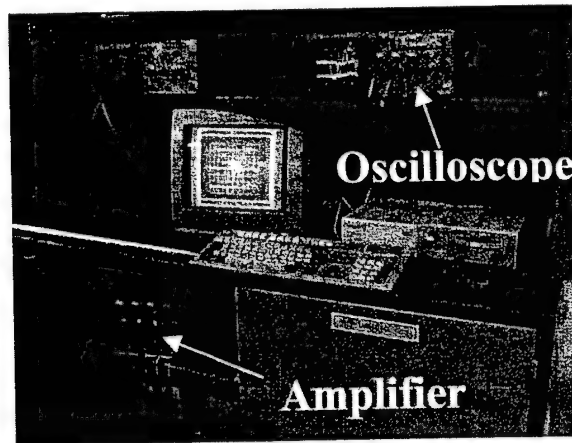


Figure 13: Amplifier, oscilloscope and computer used in the Hopkinson bar tests

The grips used for these tests were special grips designed to test fabrics. The felt was protected with Kevlar to ensure that the direct contact with the steel of the wedge did not weaken it.

There are two important limits when using a Hopkinson bar: the first one is the resolution, which is limited by the oscilloscope, and the material used to build the Hopkinson bar, this limitation was partially solved with the use of an aluminum output bar. The second important limitation is the size of the pulse generated by the incident projectile. Our Hopkinson bar generates a 100 μs pulse, which is not long enough to break the specimen tested. The longer the projectile is the longer the pulse is generated. In these tests, even if the specimens used were very small to facilitate equilibrium in the specimen, the projectile was not long enough to have time to break the specimen before the pulse was exhausted. The specimens were 13 mm wide and 10 mm long. The same specimens were used in some of the static tests for comparison. The maximum load observed in the dynamic tests is not consequence of the failure of the specimen but to the end of the loading pulse, as it was remarked in the post-mortem analysis. The strain rate in the Hopkinson bar test is approximately 10^3 s^{-1} .

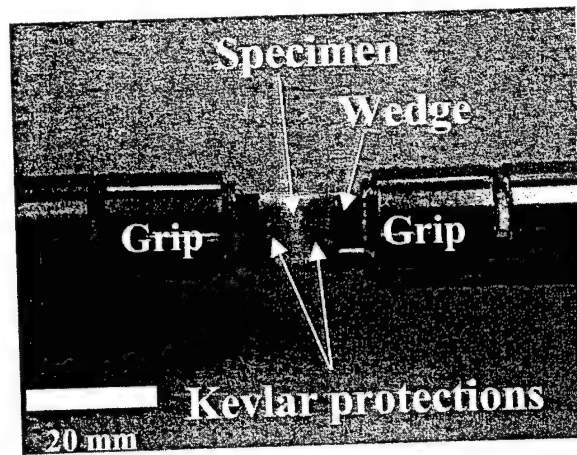


Figure 14: A specimen mounted in the Hopkinson bar before the test

Considering the length of the pulse ($100 \mu\text{s}$) and the speed of the input bar (20 m/s) it is possible to estimate that the displacement obtained in the specimen before the pulse begins to decrease is 2 mm , or roughly 20% strain for the specimen. In fact it was found that only the first 10% part of the stress-strain curve was reliable.

Test Results

Eight tests were performed in the Hopkinson bar of the department, five with steel bars and three with an Aluminum output bar. The specimen is drawn in Figure 15. The direction of the application of load was the transverse direction of the Dyneema roll (the stiffer one).

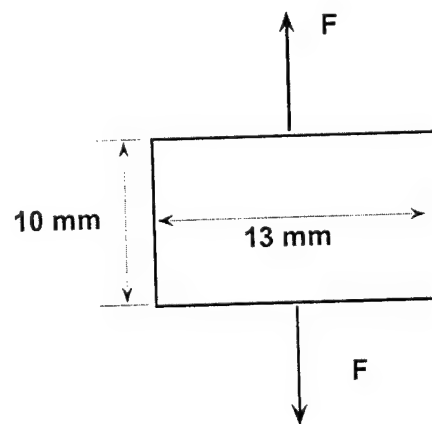


Figure 15: Diagram of the Hopkinson bar specimen.

Figure 16 is different from the one presented in the interim reports because, by using the Aluminum bar it was understood that the pulse decays when the strain in the specimen is around 10%, i.e. long before breaking it. Figure 16 shows the eight tests performed with the Hopkinson bar together with two of the static tests performed with the same grips and specimens. The tests performed with the Steel Hopkinson bar have been smoothed because the noise was hiding the signal (the amplification used was around 3000). With the aluminum bar the background noise was reduced to 20 Newton. Consequently the tests done with the Aluminum Hopkinson bar did not need any smoothing. The specimens used for the Aluminum Hopkinson bar tests were pre-stressed to 500 N to try to go a little further in the stress-strain curve, but in fact all the specimens stretched and relaxed before the beginning of the experiments.

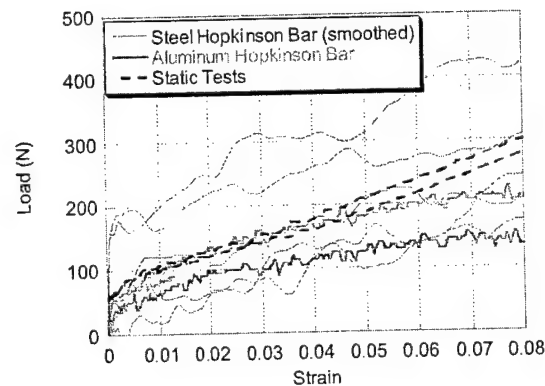


Figure 16: Comparison of the results obtained in the Hopkinson bar and in the static tests

Figure 17 depicts the specimen after the test. The reader should not misunderstand the following point: the specimen fails at every single test, but for the data registered to be valid the specimen needs to break with the first pulse received. In these tests the specimen was failing after many successive waves transits.



Figure 17: A specimen after the Hopkinson bar test.

The only way to solve this problem is to use a longer projectile. If we need a pulse 5 to 10 times longer the projectile should be 2.5 to 5 times longer, which means a complete new redesign of the Hopkinson bar.

Analysis

Although the results only cover a small piece of the stress-strain curve, it is possible to confirm that the dependence with strain rate in that range is not important, since the average stress-strain curve at high velocities is similar to the static stress-strain curve. It would be interesting, maybe as future subject of research, to try to obtain the whole stress-strain curve.

The Aluminum Hopkinson bar was also used as a method to estimate the sound velocity in the felt. A long specimen (1 meter long, 13 mm wide) was used, as it is shown in Figure 18. The strain gages of the Hopkinson bar allow, with the help of an oscilloscope, to measure the time taken for a wave to go from the input bar to the output bar. The delay of the pulse caused by the grips was estimated with the testing of well-known materials (aluminum). Preliminary tests seemed to show that the sound velocity in the Fraglight was a function of how much the material was previously pre-strained. Consequently tests were performed with different pre-strains levels.



Figure 18: Measuring the sound velocity in the felt with the Hopkinson bar

The sound velocity in the specimen as a function of the pre-strain is shown in Figure 19. The circles are the experimental results shown with a linear fit. The sound velocity increases linearly from 600 m/s to around 4000 m/s with the pre-strain. The high speed

photography gave a sound velocity of 600 m/s in unstrained material confirming that the values obtained in the Hopkinson bar are reasonable, and that "strange" results obtained in previous reports (2000 m/s sound velocity) are compatible with the felt as long as it is pre-strained.

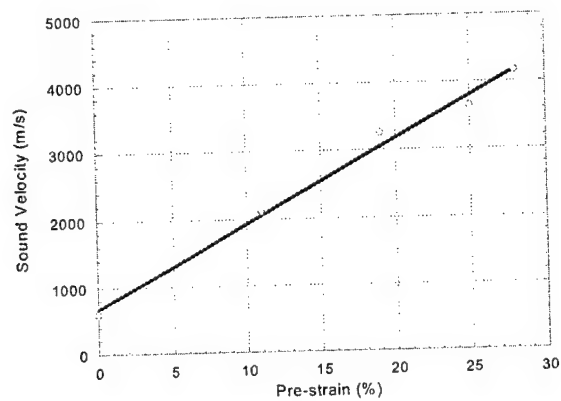


Figure 19: Sound velocity as a function of the pre-strain

2.2.7 Out-of-Plane Testing

Introduction

The out-of-plane behavior of a ballistic fabric or a felt results of great interest because the load-deflection curve might be useful when modeling numerically or analytically the penetration process. As in the tensile testing, the results of the out-of-plane punching (OOP) tests depend on the boundary conditions and might also depend on the velocity of application of the load.

Two parameters were varied during the OOP tests. The first was the size of the sample, the sample varied from 20 to 80 mm in diameter. This would allow us to evaluate a size effect similar to the one studied in the tensile testing phase. The other variable studied was the strain rate, or, in other words, the velocity of the punching device. The test procedure, the results and a discussion of the results follow introduction.

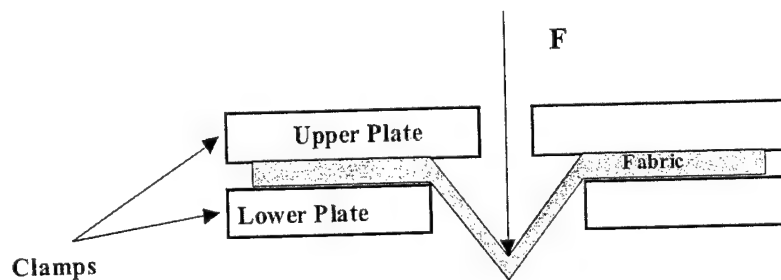


Figure 20: Diagram of an Out of Plane test

Test Description

The test is depicted in Figure 20. A tup presses with force "F" the center of a circular specimen, which is clamped between the upper and lower plate. Figure 21 shows the actual setup in the INSTRON testing machine. The specimens used were one-layer disks of non-woven Dyneema with a constant diameter of 95 mm. The effective diameter tested was that of the lower clamp, since it was verified during the experiments that the fabric could not slip in between the clamps (Sixteen bolts were used to clamp the specimen between upper and lower plate, see Figure 22).

The force F depends on the diameter of the hole of the lower plate and on the amount of deflection. The tup has a hemispherical nose, 13-mm diameter. Four different lower

plates were manufactured with 20, 40, 60 and 80-mm diameter holes. The reader can find the drawings of the plates in the annex of previous interim reports.

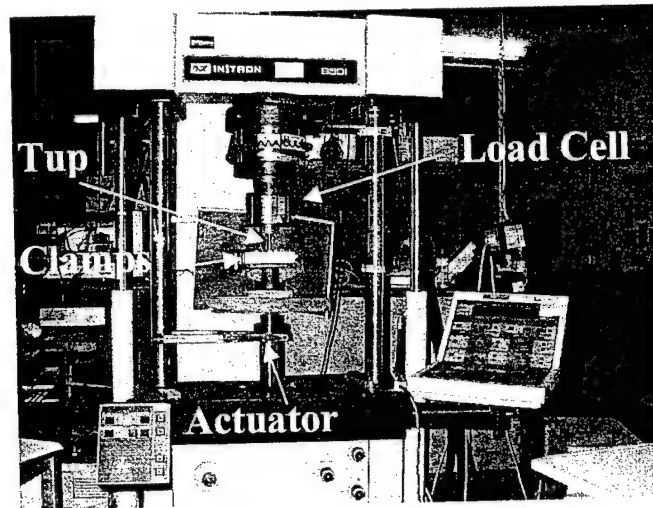


Figure 21: Set-up of Out of Plane tests.

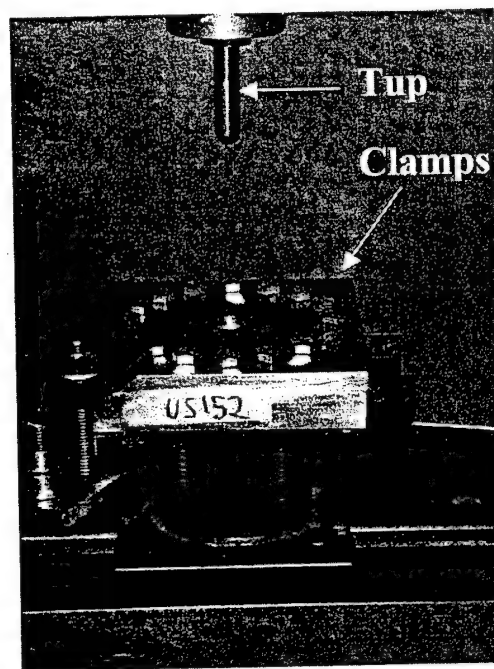


Figure 22: Close view of tup and clamps

Test Results

Each configuration was tested three times in the same conditions to check the dispersion of the results.

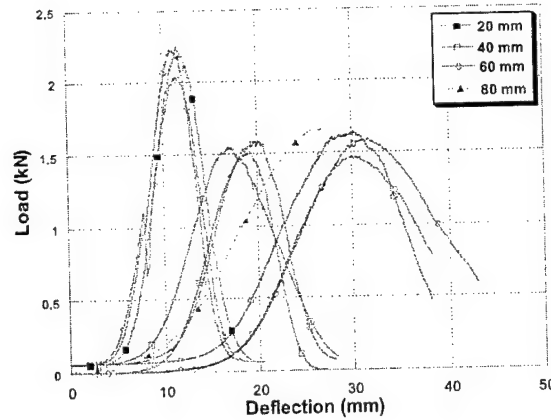


Figure 23: Size effect in the out of plane testing (5 mm/min)

Figure 23 plots the results for 20, 40 60 and 80 mm diameter (the tup moving at 5 mm/min) showing that the force needed to perforate (force at failure) the 40, 60 and 80 mm diameter specimens is very similar, while the force needed for the 20 mm diameter specimen is much higher.

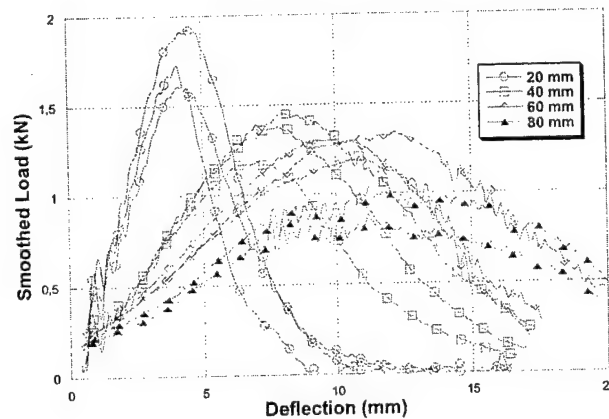


Figure 24: Size effect in the out of plane testing with drop weight machine (3.6 m/s)

The size effect in the load-deflection curve is also presented (Figure 24) for the high speed tests performed with the Drop Weight Testing machine (brand name Dynatup). In

these “dynamic” tests the maximum load decreases with the size of the specimen, although it is pointed out that the dispersion in these tests is higher than in the static ones.

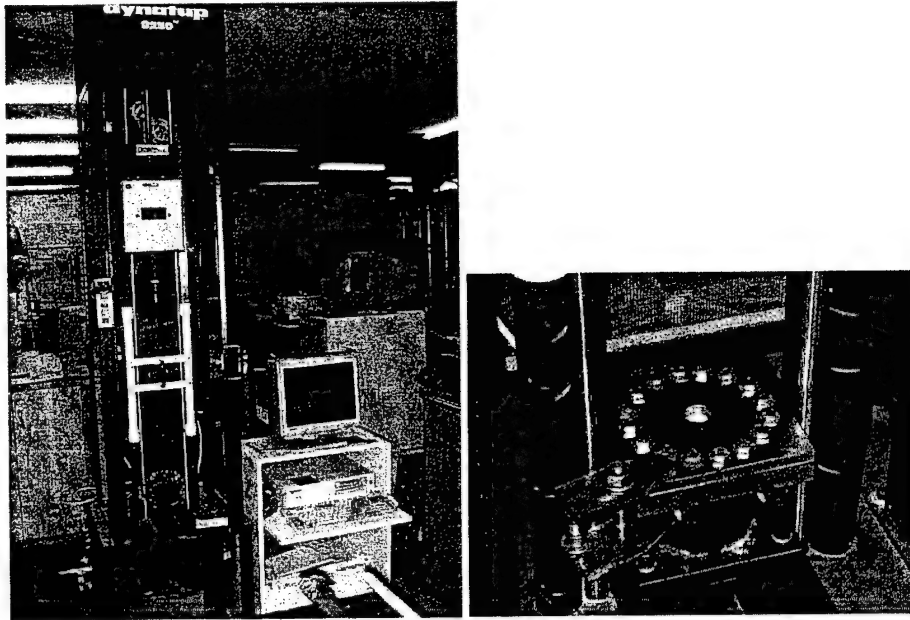


Figure 25: The Drop Weight Tester and the specimen mounted inside it.

To study the strain rate effect in these specimens, tests were performed at two different actuator velocities (5 mm/min and 500 mm/min) with an Instron testing machine and a Drop Weight testing machine. The weight dropped was 22.5 kg from 0.72 m height. The velocity of the tup at impact was 3.7 m/s, testing the fabric at 3700 mm/s or 222000 mm/min, three orders of magnitude higher than the Instron machine. Figure 26 shows the result for the 20 mm diameter specimen. The maximum load obtained is similar in all the range of velocities. Also the slopes are very similar, the maximum deflection seems smaller at high velocities, although in reality the curves are actually only shifted because the data acquisition system in the Instron machine begins to record data long before the load begins to increase. Similar conclusions were drawn from the results obtained for the other specimen sizes, as shown in Figure 26 through Figure 28.

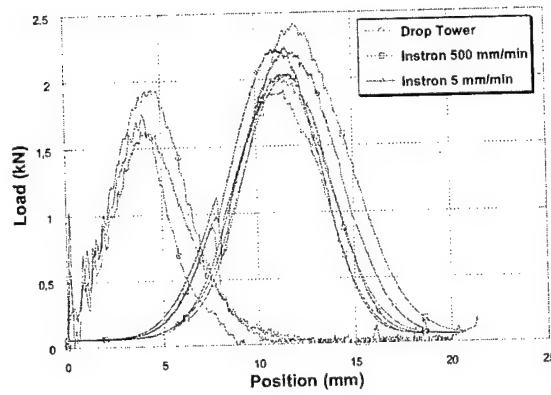


Figure 26: Strain rate effect in a 20 mm diameter specimen

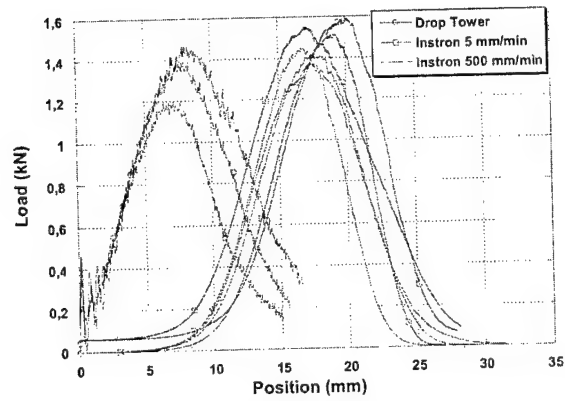


Figure 27: Strain rate effect in a 40 mm diameter specimen.

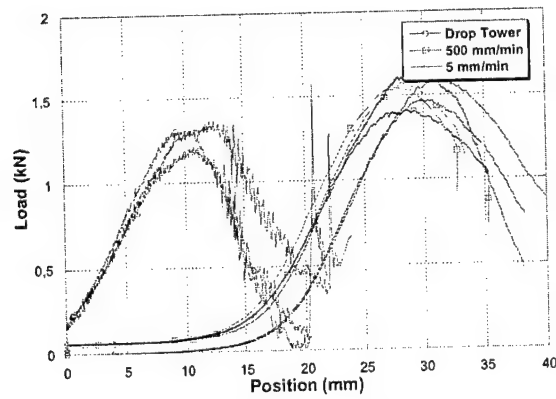


Figure 28: Strain rate effect in the 60 mm diameter specimen

Analysis

The out-of-plane tests confirm the results obtained with the tensile tests: if a specimen is bigger than 40 mm its behavior is characteristic of this material, i.e. the load at failure for a 40-mm specimen is the same than for a 60 or 80-mm (and most likely even larger) specimens. These tests also confirm that the strain rate effect, for the range from static to 4 m/s velocities, is not significant.

Figure 29 shows a specimen before being tested. The line drawn in it is the transverse direction to the roll; the fibers are mainly aligned in that direction. The shape of the deformed specimen is conical, but the base of the cone is not a circle but more likely an ellipse, due to the anisotropy of the felt. The deflection is larger in the transverse direction of the roll.

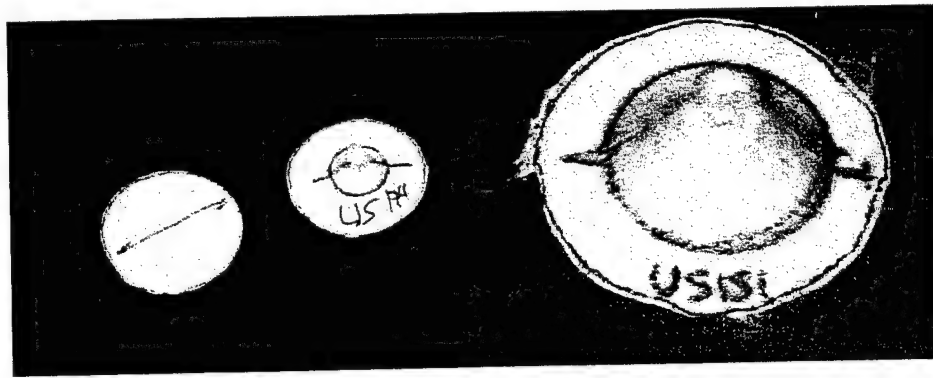


Figure 29: a) A specimen before and after being tested with the 20 mm diameter clamp. b) A close view of a specimen tested with the 60 mm clamp.

2.2.8 Summary

The main conclusions from the mechanical testing are:

- 1) The Polyethylene fiber is linear elastic until failure, i.e. essentially brittle.
- 2) The non-woven Polyethylene is very non-linear, non-isotropic with plasticity (meaning non-recoverable deformations) and softening.
- 3) The non-woven felt properties are strongly dependent on size, load direction and temperature
- 4) The non-woven felt properties do not vary remarkably in the range of strain rates from 10^{-3}s^{-1} to 10^3s^{-1} , although more work would be needed in the high strain rate regime.
- 5) The two previous conclusions are still valid for out-of-plane tests.

2.3 Ballistic Testing

2.3.1 Introduction

Ballistic testing is a key point in this research since it allows to obtain data that are controlled, knowing all the boundary and initial conditions that afterwards will be needed to perform numerical simulations with confidence. First the procedure of the tests will be described. Secondly the results of the tests, i.e. ballistic limits and residual velocity vs. striking velocity curves, will be presented. The number of layers of Dyneema felt tested was from one to three, and the projectiles were the 17-grain and 4-grain FSP. Some of the impacts were oblique (at 45 degrees). In eight tests high-speed photography was used to track the deformation of the target.

2.3.2 Test Procedure

One to three layers panels (53 cm x 53 cm) were shot with 1.1-gram (17-grain) and 0.25-gram (4-grain) fragment simulating projectiles. For the two and three layers configuration the stacking sequences were, respectively, 0/90 and 0/90/0. The projectile was accelerated to a maximum velocity of 750 m/s by a Helium gas gun. Figure 30 shows a general view of the gun system, with the two velocity panels used to measure the striking velocity.

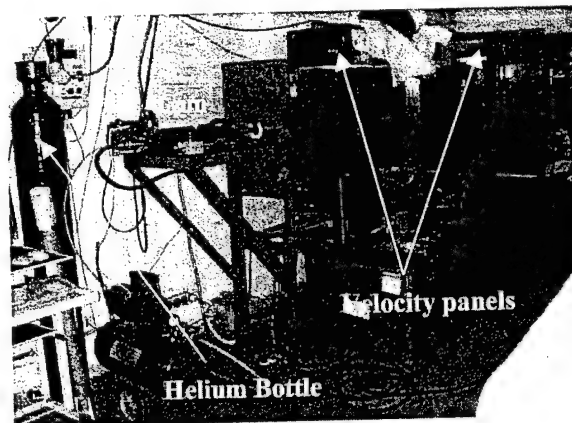


Figure 30: Set-up of the shooting tests.

To measure the residual velocity the steel projectile passed through two aluminum foil switches after penetrating the non-woven felt. The perforation of the first switch triggered a "low" signal in an oscilloscope and the perforation of the second switch a

“high” signal. The square pulse registered by the oscilloscope directly gave the time taken by the projectile to travel from the first to the second switch. Unfortunately it was impossible to register directly the closing of the aluminum circuit because it was not a clean closing, but the signal bounced many times producing erratic records in the oscilloscope. The problem was solved by using a 555 integrated circuit (per switch) that produced a clean (exponential) rise of a signal as soon as it received a slope. The signals of both 555 integrated circuits were logically added with a 7400 that generated a non-ambiguous output. Figure 31 is a photograph and drawing of the circuit utilized. Benchmark tests were performed without target to compare the velocities measured by both the velocity panels and the switches. The velocities were basically identical within a 5% margin.

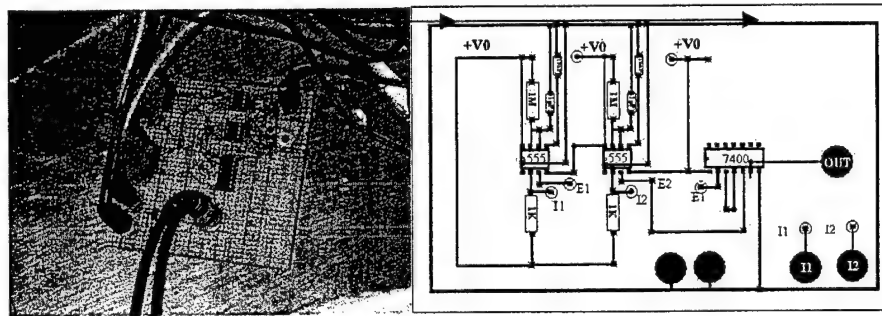


Figure 31: Photography and drawing of the circuit used to measure the residual velocity

One of the big concerns during these tests was to set them up in a way that, afterwards, could be easy to simulate numerically. In particular the boundary conditions might change significantly the residual velocities and ballistic limit of the felt. Many options were considered, like clamping the felt around the borders or leaving it hanging completely unconstrained. It was decided not to clamp the felt around its borders since this would not be a “clean” boundary condition: slippage and the friction coefficient between the felt and the frame would become additional problems to the simulations. Leaving the felt hanging completely unconstrained was not an option either, since at impact velocities close to the ballistic limit the felt would literally fly with the projectile. Instead of it a wood frame was used (see Figure 32) leaving the felt as unconstrained as possible: the lateral borders were free and the upper and lower boundaries were only constrained in the X direction (the direction of the velocity), since the wood used to hold the felt was loose. This condition can be easily simulated

numerically, since the felt might be considered completely unconstrained or, if necessary, its lower and upper end horizontal motion can be set to zero. Afterwards it was checked that the numerical simulations were not sensitive enough to appreciate any difference in the ballistic limit between the two boundary conditions mentioned.

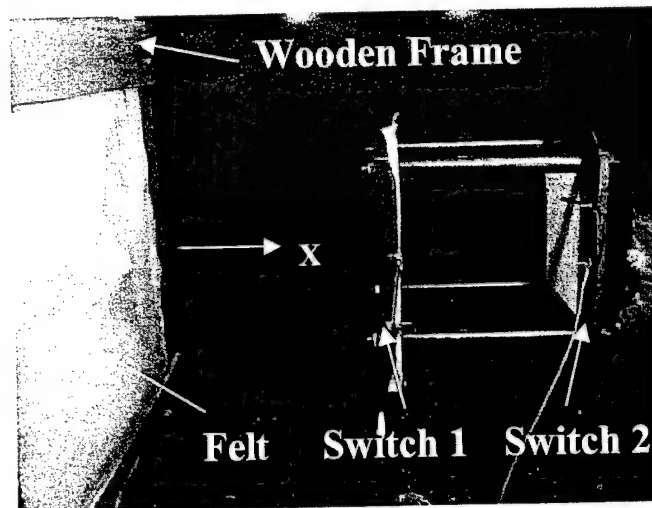


Figure 32: Wooden frame and residual velocity measurement device.

The high speed photographs were taken with four PCO CCD cameras. The minimum exposure time with these cameras was $1 \mu\text{s}$. The four cameras aimed at a PMMA mirror where the back of the target was reflected (see Figure 33).

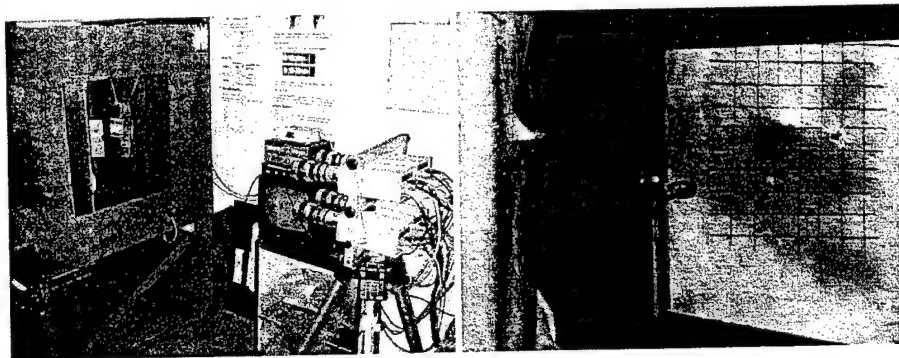


Figure 33: Set-up of the four CCD cameras and mirror used to track the back of the target with high-speed photography.

2.3.3 Results for the 17-grain FSP

Figure 34 shows the residual velocity vs. striking velocity curves obtained with a total of 28 good shots. The circles, diamonds and squares are actual tests measurements. The tests were fitted with curves that follow the Lambert equation:

$$V_r = (V_s^n - V_{50}^n)^{1/n}$$

The ballistic limits were 290 m/s for the one layer configuration, 365 m/s for the two layers and 460 m/s for the 3 layers. The “n” coefficients used for the fitting were, respectively, 3, 3.5, 4.

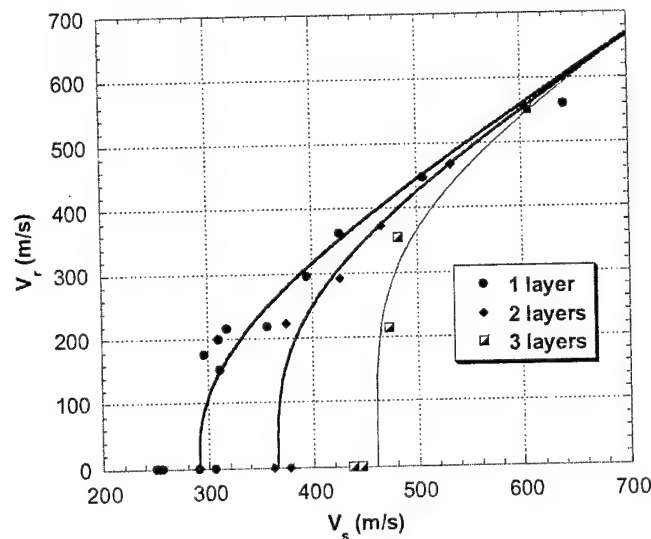


Figure 34: Residual velocity vs. Striking velocity for the 17-grain FSP impacting normally 1 to 3 layers of non-woven Dyneema

Three layers configuration was used to compare the performance of Dyneema Fraglight at oblique (45 degrees) and normal impact the because the difference for one or two layers systems would be unnoticeable. Figure 35 shows, unexpectedly, that Dyneema Fraglight behaves worse (less protection, lower ballistic limit) when the impact is oblique than when the impact is normal. This is a new phenomenon for the authors since metallic and Kevlar [1] targets usually increase their V50 when impacted obliquely. It is important to mention that the dispersion of the results in the oblique configuration is much bigger than that in the normal configuration. The ballistic limit was estimated to be 390 m/s.

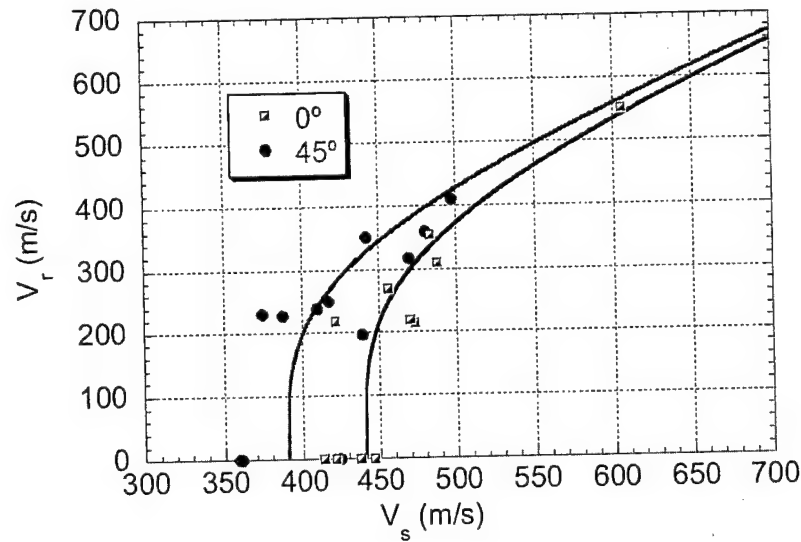


Figure 35: Residual velocity vs. striking velocity for normal and 45° impact of the 17 grain FSP into three layers of non-woven Dyneema.

2.3.4 Results for the 4-grain FSP

New devices to measure the residual velocity had to be designed because the old ones did not work with such a small projectile. One, two and three layers of Fraglight were shot at normal impact. The stacking sequence was 0/90 degrees for the two layers specimen and 0/90/0 degrees for the three layers one. The results of the shooting tests with 1, 2 and 3 layers are presented in Figure 36.

The ballistic limits for the one, two and three layers configurations were respectively 375 m/s, 475 m/s and 510 m/s. Figure 36 also shows the Lambert fit for each one of the residual velocity curves. The ballistic limit of the one layer configuration is only estimated; it was not possible to shoot at lower velocities than 375 m/s (pressures under 20 bar) in our gun.

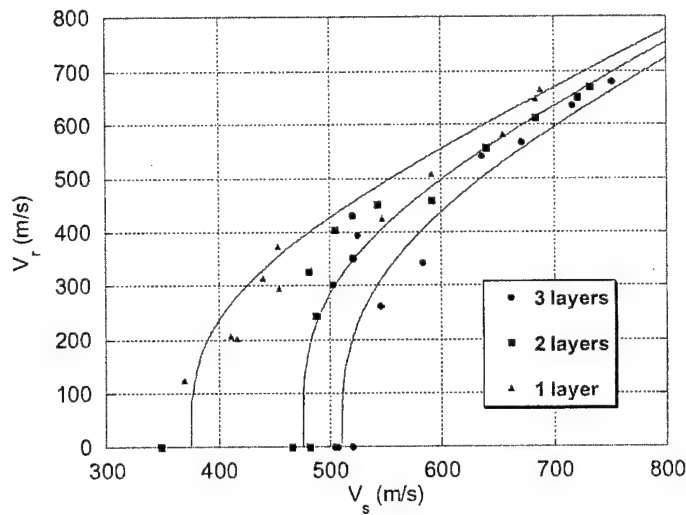


Figure 36: Residual velocity vs. striking velocity of the 4-grain FSP for 1,2 and 3 layers of Fraglight

2.3.5 High Speed Imaging of the back of the target.

The objective of the project is to simulate the penetration process of a fragment into the non-woven felt. In order to assess a numerical simulation, high speed imaging of the penetration process is extremely useful. A good numerical simulation should be able to reproduce the wave propagation process in the felt, i.e. longitudinal and transverse waves. Ideally it would also predict residual velocity, ballistic limit and the history of the penetration. Unfortunately the position of the projectile as a function of time during penetration is very difficult to track with only four CCD cameras, thus the assessment of the numerical models will rely mainly on wave propagation and residual velocities.

Figure 37 shows four consecutive photographs (one single gun shot) taken when a 17 grain FSP is shot at 361 m/s against a *single* layer of Fraglight. The panel is free in the air (no clamping) and its size is 70 cm x 70 cm. Two waves propagate in the fabric: 1) A wave transverse to the felt that forms the non-symmetric cone which vertex is the projectile (that causes the deflection of the felt). 2) A longitudinal wave that travels faster and makes the fabric particles move radially towards the impact point.

Line (1) in image (b) shows the front of the longitudinal wave propagating in x direction. The front has moved up to line (2) in image (c). From the images (b) and (c), it is possible to see the longitudinal wave is moving approximately at around 600 m/s (3 centimeters in 50 μ s). This value agrees with the value that can be calculated from

the stress-strain curve where the slope gives a value of around 560 m/s to 720 m/s. Of course this value is very rough, but gives important information for future numerical simulations. The transverse wave (it is the cone) moves approximately at half the speed (300 m/s) in the x direction, when measured between images (b) and (c). In the y direction transverse waves travel at around 150 m/s. Longitudinal waves in the y direction are difficult to observe in this images, although it is evident from image (d) that they go faster than transverse waves, and a rough estimation could be 300 m/s. It is also important to observe that the transverse wave slows down during the impact. Image (d) is taken at a very late time so the transverse average velocity between (c) and (d) is 150 m/s.

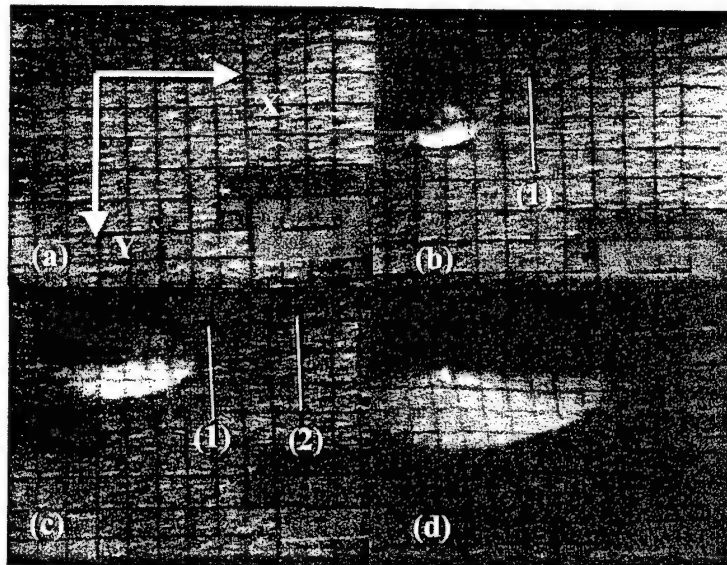


Figure 37: Photographs at 0, 40 μ s, 90 μ s and 290 μ s. Striking velocity 361 m/s. One layer

Figure 37 shows the back of a two layers panel. The two layers are stacked at 0 and 90 degrees to obtain a more symmetric response. As expected, a pyramid develops during the impact, but the pyramid is not completely symmetric. The transverse wave is faster in the x direction than in the y direction. Sound speed is still around 600 m/s in the x direction (measured from line (1') to line (2')). Transverse waves, from images (b') and (c'), travel at a similar speed than the ones in Figure 37. The reader can find six more high speed images in the annex of the interim reports.

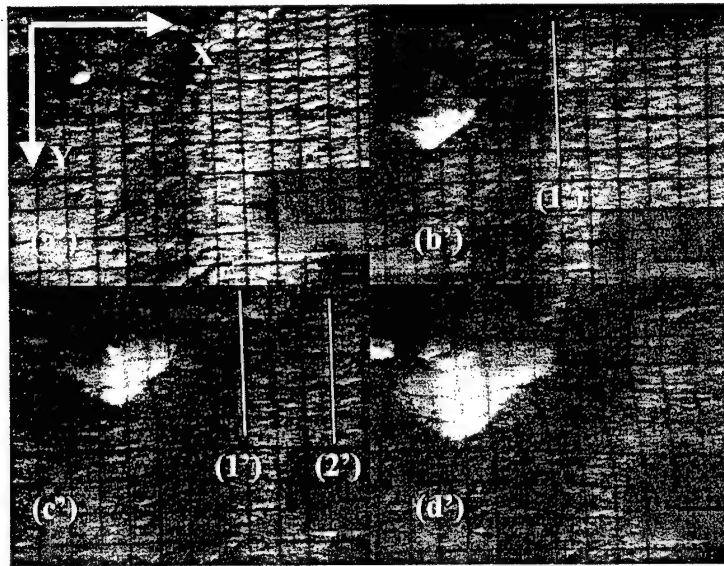


Figure 38: Photographs at 0, 45 μ s, 95 μ s and 235 μ s. Striking velocity 524 m/s. Two layers

2.3.6 Discussion and Summary

Table 1 summarizes the ballistic limit for all the configurations tested. With the boundary conditions described above, 3 layers of Fraglight have a ballistic limit of around 450 m/s when shooting with the 17-grain FSP (normal impact), as shown in Table 1. DSM, the manufacturer of the felt, states in the properties sheet of Dyneema Fraglight that 6 layers (1.2 kg/m^2) are needed to obtain that same performance. Probably the manufacturer is giving a design well in the safe side to account for both the dispersion of the results and the fact that the felt decreases its performance under oblique impact.

	17-grain FSP		4-grain FSP
	Normal	45 degrees	Normal
One layer	290 m/s	NA	375 m/s
Two layers	365 m/s	NA	475 m/s
Three layers	460 m/s	390 m/s	510 m/s

Table 1: Ballistic limit for the configurations tested.

The anisotropy is probably the cause of the decrease in performance under oblique impact. If we imagine a single unidirectional layer (all the fibers with the same direction) it is easy to understand that depending on the orientation of the layer the

ballistic limit can change: Figure 39 a) shows an oblique impact, but with the velocity contained in a plane perpendicular to the fibers and Figure 39 b) shows an oblique impact with the velocity of the projectile contained in the plane of the fiber. Case b) would give a lower ballistic limit because the fibers impacted are stretched non-symmetrically, while the fibers of the fabric shown in a) are stretched symmetrically.

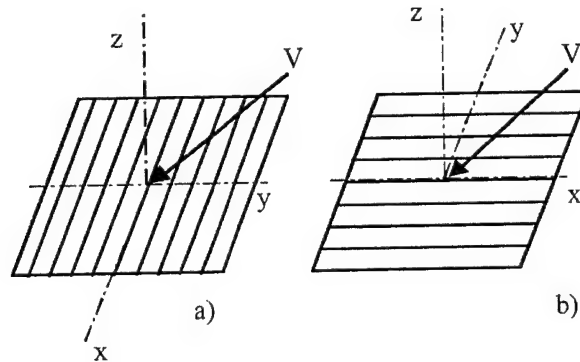


Figure 39: Two possibilities in an oblique impact into a unidirectional layer: a) velocity contained in the plane perpendicular to the fibers, b) velocity contained in the plane of the fiber.

The felt used in this contract is not unidirectional, but it is very anisotropic, with the fibers mainly aligned in the direction transverse to the roll, so a similar effect is thought to be present.

3 Numerical Simulations

3.1 Introduction

The mechanical characterization of Fraglight has shown many of its peculiarities:

- 1) Size dependence : small specimens (length=1 cm) are stiffer than big specimens (length=5 cm or more)
- 2) Big specimens have a high strain to failure (up to 50%)
- 3) Apparently the elastic behavior is non linear.
- 4) The material softens after failure.
- 5) The Fraglight received is orthotropic.
- 6) Probably there is no plastic behavior (the polyethylene fiber is linear elastic until failure), but irreversible disentanglement of fibers.

These peculiarities are due to the way the Fraglight is manufactured: short fibers (5 cm length) mainly aligned in the transverse direction of the roll. All these characteristics make the numerical simulation of the impact extremely difficult since the material is not even continuum and it is not clear which of the properties (the small specimen properties or the large specimen properties?) are the appropriate to perform the simulation.

To gain insight in the material properties some simulations of the static tensile tests were performed with the help of the finite element code ABAQUS. The main objective of these simulations was to find a Poisson's ratio needed for the dynamic simulations with AUTODYN. However they turned out to be also useful to estimate the elastic moduli. Afterwards, the static properties found with ABAQUS were used in the dynamic simulation of the shots with AUTODYN 3-D and 2-D, but the residual velocities were very far from the experimental ones. The only way to obtain reasonable residual velocities was to stiffen the felt to values close to the ones of the fiber, as it will be shown below.

3.2 Numerical Simulations of static tensile tests with ABAQUS

Only the specimens of 100 mm x 100 mm were simulated. The Load per length vs. True strain curves and the photographs taken during the static tests were used to compare numerical and experimental results.

Figure 40 shows with thin lines the Load vs. Strain curves obtained in the mechanical characterization tests. The thick lines are the same curves but obtained numerically with ABAQUS using the following properties:

- 1) Orthotropic material
- 2) Linear elastic until failure
- 3) Transverse (to the roll) elastic modulus: $E_T = 60 \text{ MPa}$
- 4) Longitudinal elastic modulus: $E_L = 4 \text{ MPa}$
- 5) Shear Modulus (in plane): $G = 2 \text{ MPa}$
- 6) Poisson's coefficient: $\nu = 0.2$

The high strains (non-linear) option of the ABAQUS was used. Neither plasticity nor softening was included in the calculation. Figure 40 compares both the numerical and experimental Stress – Strain curves showing a very good agreement for the transverse (a), 45 degrees (b), and longitudinal (c) tests. Figure 41 shows the deformed shape for all the three configurations, which is also in very good agreement with the tests seen in Figure 42.

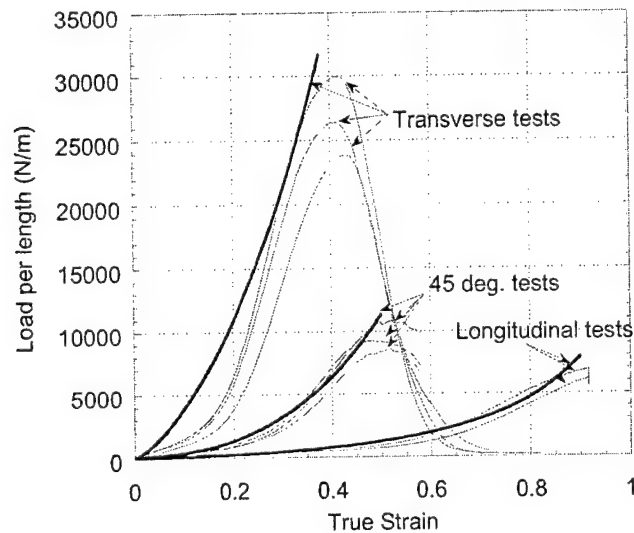


Figure 40: Load per Length vs. True Strain Curves for three different directions. Thin lines are the real tests while thick lines are the predictions calculated with ABAQUS.

3.3 Numerical Simulations of the impact of FSPs with Autodyn 3D

Autodyn 3-D has important limitations when modeling a felt like the one studied in this project. First a Eulerian mesh is not available in 3-D, so a Lagrangian mesh is needed together with its corresponding erosion model to remove the cells that are greatly distorted. Since the thickness of the felt is so small (around 0.25 mm), putting elements through the thickness gave unrealistic results: the elements were so distorted during the calculation that they were eroded too soon. The problem suggests that a membrane mesh might be adequate, but Autodyn does not allow the use of an orthotropic material with a membrane. In fact qualitatively good results for the wave propagation were obtained with a Lagrangian mesh with five elements through the thickness, and a linear elastic model, but the residual velocities were not well predicted, after trying a wide range of material properties, because of the erosion problems already mentioned.

Another problem was related to the mechanical properties that should be used in the numerical simulations. Should the properties found in the tensile testing of the small specimens be used? Or should the ones of the big specimens be used? This two-scale problem (in fact multiple scale) is impossible to simulate with the usual continuum mechanics models used in the finite difference codes. The only way to simulate something similar to the two-scale phenomenon, without writing complex user subroutines, was to define a stiff area in the felt around the projectile and a soft area far from it using a membrane mesh. This was done and explained in the fifth interim report, but the results were unsatisfactory. Probably only non-local models would be able to predict both the static and ballistic results, but those models are difficult to develop and implement and are out of the scope of this work, which tries to gain understanding of the felt with the aid of simple models.

In summary, all the models tried in Autodyn 3-D were unable to reproduce reasonable experimental results so it was decided to try to obtain an "equivalent" two-dimensional felt, which should not be essentially different from the real one and would help to obtain numerical predictions. The next paragraph of this chapter describes this effort, while the last paragraph shows the results obtained with LS-DYNA, which allows the use of a membrane mesh with orthotropic material.

3.4 Numerical Simulations of the impact of FSPs with Autodyn 2D

The 2-D calculations were performed with a shell mesh (100 nodes) with axial symmetry and isotropic material. The material properties adequate to reproduce the Residual Velocity vs. Striking Velocity and the deformed shape of the Fraglight were the subject of an intensive research. The first calculations included very simple linear elastic material models. These models were progressively modified to introduce new features like plasticity, failure and dependence of strain rate of the modulus, yield strength and strain to failure. The "benchmark" test used to compare the experimental and numerical results was the 17 grain FSP impact at a striking velocity of $V_s = 400$ m/s. The residual velocity obtained in this test was 300 m/s.

a) Elasto-Plastic Model of Fraglight:

The first material properties used in the AUTODYN 2-D were the ones estimated with the ABAQUS static simulations (linear elastic up to failure), but these properties were too soft to slow down the projectile. Once it is known that the static properties are not useful to model the impact it is necessary to sweep possible properties that could reproduce the impact phenomenon. Figure 43 shows the history of the 17-grain Fragment Simulating Projectile shot at 400 m/s for different values of Fraglight bulk modulus K . The range of bulk moduli tried ranges from $K=60$ GPa, corresponding to an elastic modulus of 100 GPa, the modulus of the Polyethylene fiber (the value of the Poisson's ratio is assumed to be 0.2), to $K=0.06$ GPa, the value found in the static tests. The Yield strength assumed (Von Misses criterion) was $Y=1$ GPa, measured in the tensile tests of the small specimens.

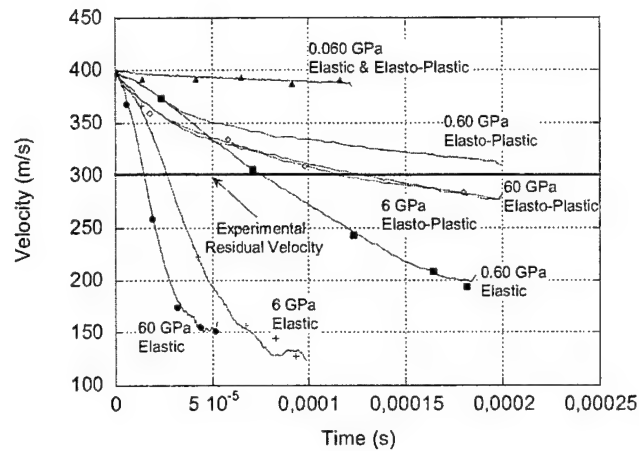


Figure 43: Determination of the material parameters that could possibly reproduce the impact. All the calculations are for the 17-grain FSP against one layer of Fraglight

Even if the Polyethylene fiber is linear elastic until failure, from postmortem analysis of the Fraglight target it is reasonable to assume that the elastic up to failure model is not realistic because the fibers untangle during the impact. The shape of the target around the impact point after perforation is a non-symmetric cone that has suffered non-reversible deformation that could be assumed as plastic deformation. From Figure 43 it is evident that the only acceptable Bulk Moduli are $K=6$ GPa or $K=60$ GPa since the other values would never stop the projectile or would stop it in an unrealistic time scale. A value of $K=60$ GPa was selected for future calculations because it gave a slightly better prediction of the Residual Velocity vs. Striking Velocity curves for 1 layer impact. Either $K=60$ GPa or $K=6$ GPa required the Effective Plastic Strain to failure to be $\epsilon_{fail} = 5$ (or 500 %). Obviously this number is not the strain to failure of Fraglight, but the value necessary to obtain a reasonable residual velocity with an elasto-plastic model. This value might be so high because of the work performed by the projectile to untangle the fibers.

With this material model the results of the simulation for 1 layer were excellent, as shown in Figure 44.

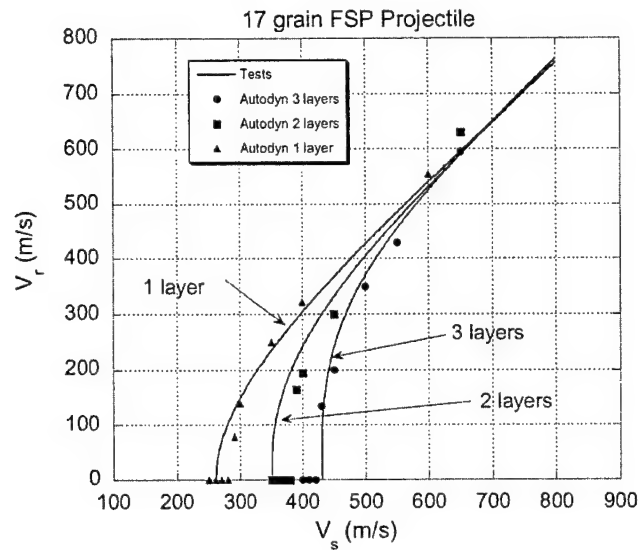


Figure 44: Residual velocity vs. striking velocity for the 17 grain FSP projectile. The curves fit the experimental results, the triangles, squares and circles are the AUTODYN predictions.

For two and three layers the results were good predicting the ballistic limit, but underestimated the residual velocity for impacts over 500 m/s (these results are not shown in Figure 44). This means that at high velocities the Fraglight takes less energy from the projectile than the energy calculated in the numerical simulations. There were two possibilities to explain this error. As it only happened with many layers, the problem was either in the interaction between the layers or in a change of the material properties at high velocities.

To check the first hypothesis the distance between the layers was modified from virtually zero to a distance where there was no interaction between the layers during the impact. The results improved scarcely when the layers were very close, but not enough to explain the difference with the tests. Besides a friction interaction between the layers was incorporated because if friction did exist it would constrain the movement of the particles of the target diminishing the energy the target could absorb. The only way to match the experimental residual velocities (shown in Figure 44) was to assume a friction coefficient of 4, which seems unphysical. Plus the error was not corrected when simulating the 4 grain FSP impact, see in Figure 45 the simulations at $V_s=650$ m/s.

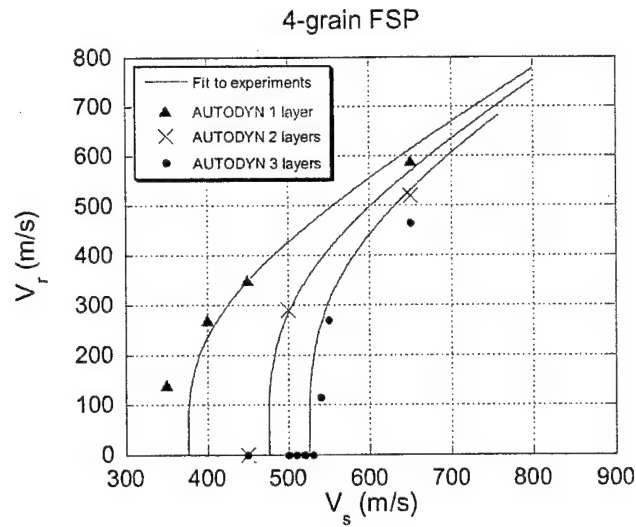


Figure 45: : Residual velocity vs. striking velocity for the 4-grain FSP projectile. The curves fit the experimental results, the triangles, crosses and circles are the AUTODYN predictions.

b) Elasto-Plastic Model of Fraglight with strain rate effects:

Since the results were not satisfactory with the previous model, strain rate effects were incorporated through user subroutines written by the authors. Three different aspects were studied: 1) Strain rate dependence of the Yield Strength, 2) Strain rate dependence of the Elastic Modulus and 3) Strain rate dependence of the strain to failure.

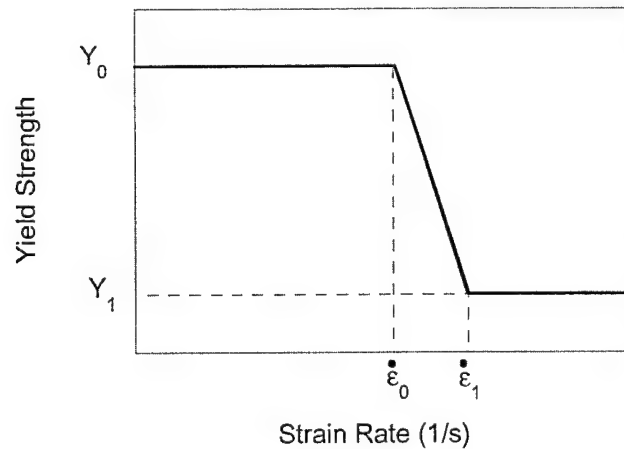


Figure 46: Example of a Yield strength model dependent on the strain rate.

Figure 46 shows an example of one of the models tried. The parameters Y_0 , Y_1 , $\dot{\epsilon}_0$, $\dot{\epsilon}_1$, were varied in a wide range to find the best match with the experiments. The transition between Y_0 and Y_1 in Figure 46 is linear, even an exponential transition was also studied giving unsatisfactory results. It might be surprising that, while usual strain rate dependent models like Johnson-Cook predict an increase in the Yield Strength with strain rate, the model presented here decreases it. The reason is that the energy absorbed by the felt at high impact velocities is smaller than at low impact velocities and if the Yield Strength is increased the energy absorbed by the felt is also increased, worsening even more the residual velocities predicted. The results of Figure 47 were obtained with: $Y_0=1$ GPa, $Y_1=0$, $\dot{\epsilon}_0 = 5 \times 10^5 \text{ s}^{-1}$, $\dot{\epsilon}_1 = \dot{\epsilon}_0$, and are the best fit that the authors could obtain with this strain dependent model.

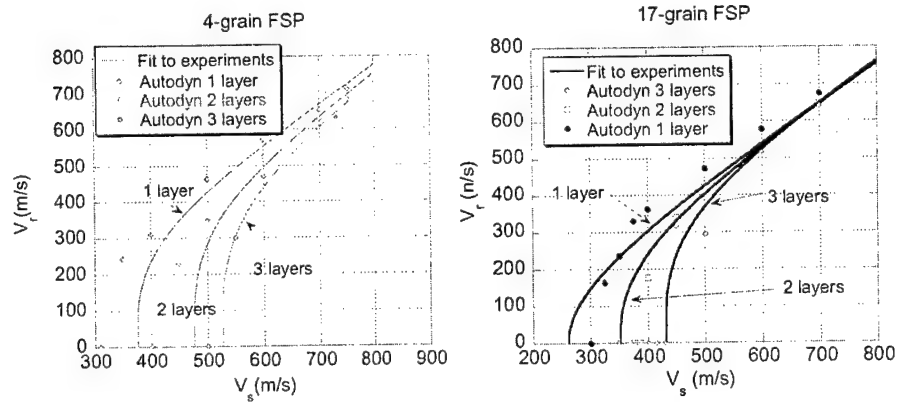


Figure 47: Results with a Yield strength strain rate dependent.

As mentioned the strain rate dependence of the elastic modulus (or bulk modulus) was also studied, but the residual velocities obtained at high impact velocities were very far from the experiments.

3.5 Numerical Simulations of FSPS impact with LS-DYNA

Since it was impossible to use simultaneously with AUTODYN a shell mesh and an orthotropic material some calculations were performed with LS-DYNA in 3-D. The mesh used is shown in Figure 48. The size is the same of the experiments (70 cm x 70 cm) and both x and y directions have the same treatment in the mesh.

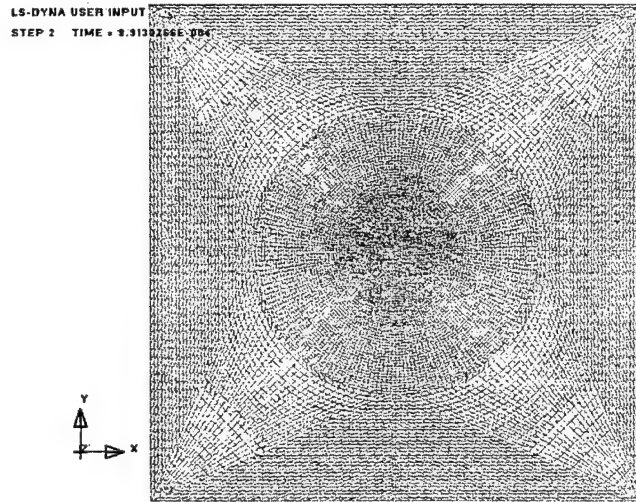


Figure 48: Shell mesh used in the LS-DYNA calculations.

The qualitative results with LS-DYNA (Figure 49) are very good, and it is possible to reproduce the wave propagation quite accurately (test in Figure 37), however LS-DYNA does not allow failure of an orthotropic material. Consequently it was not possible to obtain V_r - V_s curves to check the material model used:

$$E_y=100 \text{ GPa}, E_x=3.5 \text{ GPa}, G=2.0 \text{ GPa}, \nu=0.2$$

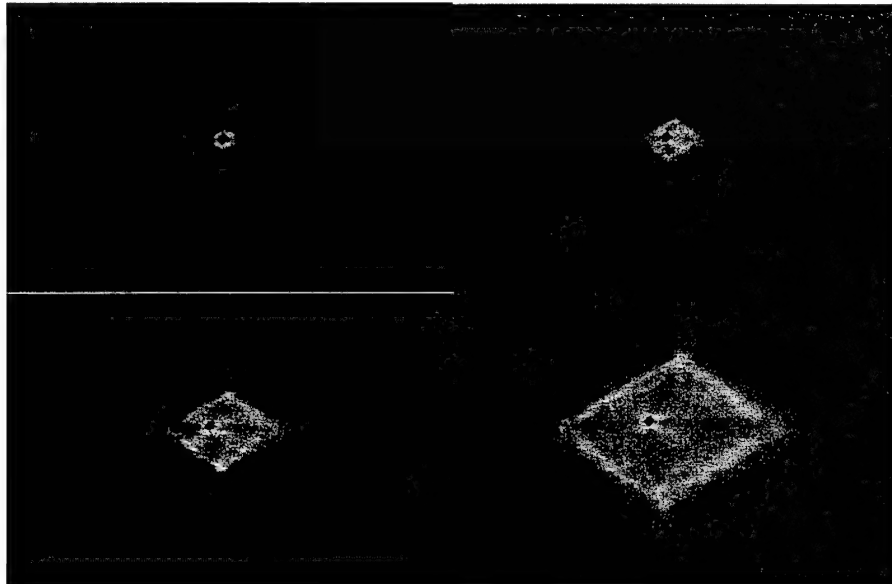


Figure 49: Sequence of the impact of 17 grain FSP into 1 layer of Fraglight seen from the back.

3.6 Summary and Conclusions

Numerical modeling of the non-woven felt has proved to be very difficult. The problems come from many fronts. First the material is non-homogenous, with an important size effect. Second the material is orthotropic, with a very small thickness, which makes it impossible to simulate if the mesh used is not a membrane. Even after a thorough mechanical characterization and the simulation of the static tests, the constitutive equation obtained still does not seem to be very realistic. Because of all these problems the objective of this chapter was finally not to simulate the real problem of impact of an FSP in Fraglight, but to obtain an homogenous, isotropic and elastoplastic material that could behave similarly to the non-woven felt in our range of interest (4 and 17-grain FSPs). At the end the experimental results were matched decently with a two-dimensional model, after introducing some strain rate dependence.

4 Analytical Simulations

4.1 *Bibliographic search and possibilities of exploitation*

The first effort in this part was to study the analytical models already available in the literature and the possibility of applying them to our problem, which is the impact of FSPs in Fraglight. The models explored were:

1) Vinson [2] proposed a membrane model for a homogenous isotropic material, 2) the semi-empirical approach by Cunniff [1] , 3) Walker [3] model for calculation of ballistic limit of Kevlar sheets 4) Chocron [4] fabric analytic model. In addition other Cunniff [5] papers were consulted.

Vinson model was rejected because it was designed for isotropic materials and Fraglight behaved very non-isotropically. Cunniff model was impossible to apply since the regression coefficients he used are specifically for Kevlar configurations, although new regression coefficients could be calculated for the Fraglight if it is found to be useful.

Chocron and Walker models were carefully studied and tried.

Chocron model was shown to be a useful tool to predict ballistic limit of unidirectional polyethylene as well as woven polyethylene armors for personal protection, but was never tried with non-woven felts. The model assumed the fabric was a collection of fibers without interaction among them, and only those fibers right under the projectile contributed to slow it down. The fibers were assumed linear elastic until failure. Failure happened through a criterion similar to Tutchter-Buller. Figure 50 shows the prediction of the model compared to the experiments. The model was in general good at predicting ballistic limits but could only predict accurate residual velocities in the 17-grain FSP, 1 layer configuration.

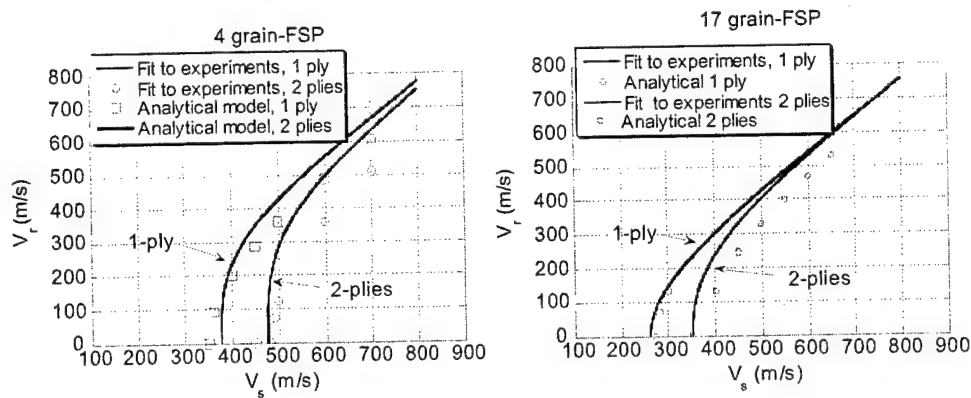


Figure 50: Comparison of Chocron analytical results and FSP experiments in the non-woven felt.

Walker model assumes that the Kevlar sheet of fabric behaves like a mesh of microscopic linear elastic springs. He finds an explicit equation for the ballistic limit that is only a function of a non-dimensional number X (which is the density of the projectile times the cross section divided by its mass), the sound velocity of the fiber (10000 m/s for the Polyethylene fiber), the strain to failure of the fiber (4% according to both experiments and data provided by DSM) and β , the area pushed by the projectile, which was forced to fit for one of the experimental results.

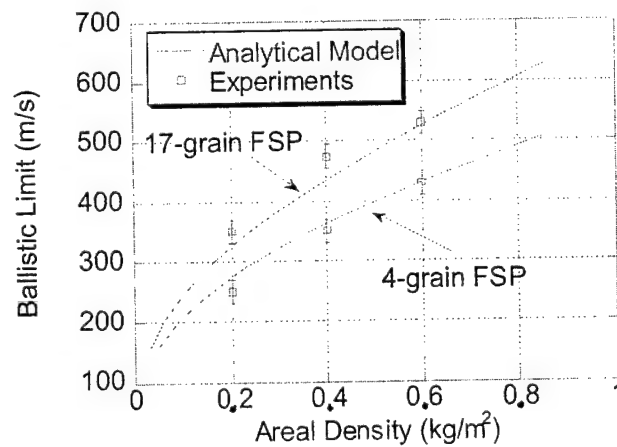


Figure 51: Comparison of Walker model results and experimental ballistic limits

Figure 51 shows that the model gives reasonable predictions, even though the model was not thought for a non-woven non-isotropic material.

4.2 Constitutive equation*

The first step in simulating analytically the impact of a bullet in a target is to have a good constitutive model of target. Once the constitutive model is available it is implemented in the equations of motion that, with the appropriate boundary conditions can give an analytic solution if it is possible to simplify them.

a) Basic Equations

Figure 52 shows the reference (K) and deformed (χ) configurations of the felt before and after being strained. $d\bar{X}$ is an undeformed vector in the reference configuration (with direction $\bar{\eta}$) of the felt and $d\bar{x}$ the corresponding deformed vector, after application of a Force. \bar{F}_f is the force along the fiber.

The relation between $d\bar{x}$ and $d\bar{X}$ is given by:

$$d\bar{x} = \bar{\bar{F}} d\bar{X} \quad (1)$$

Where $\bar{\bar{F}} \equiv \text{Grad } \bar{x}$ is the deformation gradient tensor (Lagrangian), see for instance 6.

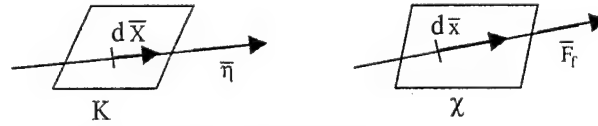


Figure 52: Reference and deformed configuration

Also, for later use, we introduce the Cauchy-Green tensor:

$$\bar{\bar{C}} = \bar{\bar{F}}^T \bar{\bar{F}} \quad (2)$$

The stretch:

$$\Lambda = \frac{dl}{dL} = \sqrt{\bar{\bar{C}} \bar{\eta} \cdot \bar{\eta}} \quad (3)$$

The force in the fiber can be written as:

$$\bar{F}_f = F_f(\Lambda) \quad \bar{e} = F_f(\Lambda) \frac{d\bar{x}}{dl} = F_f(\Lambda) \frac{\bar{\bar{F}} \bar{\eta}}{\sqrt{\bar{\bar{C}} \bar{\eta} \cdot \bar{\eta}}} \quad (4)$$

* This model was developed by Prof. Jaime Planas, from the Department of Materials Science

Where \bar{e} is a unit vector in the direction of the fiber, dL the length of $d\bar{X}$ and dl the length of $d\bar{x}$.

To find the constitutive equation let's write that the work performed by the forces per unit of volume in the deformed configuration must be equal to the work in the reference configuration:

Stress power in the deformed configuration:

$$\int_V \bar{\mathbf{T}} \cdot \bar{\mathbf{G}} dV = \int_V \bar{\mathbf{T}} \cdot \dot{\bar{\mathbf{F}}} \bar{\mathbf{F}}^{-1} J dV_K \quad (5)$$

where $\bar{\mathbf{T}}$ is the Cauchy stress tensor, $\bar{\mathbf{G}} \equiv \text{grad } \bar{\mathbf{v}}$ is the gradient (Eulerian) of the velocity field and J is the determinant of $\bar{\mathbf{F}}$, that multiplied by the reference volume gives the instant (deformed) volume.

Stress power in the reference configuration:

$$\int_V \bar{\mathbf{T}}_K \cdot \dot{\bar{\mathbf{F}}} dV_K \quad (6)$$

where $\bar{\mathbf{T}}_K$ is the Cauchy stress tensor in the reference configuration and dV_K the volume in the reference configuration

Both stress powers are the same, hence: $\bar{\mathbf{T}}_K = J \bar{\mathbf{T}} \bar{\mathbf{F}}^{-T}$

The work done to one fiber that lies along θ direction with respect to a reference direction (for example the direction transverse to the roll), per unit length is: $F_r^\theta \dot{\Lambda}$.

Let's define the volume fraction of fiber as $f_r \equiv \frac{l_r A_{Kf}}{dV_K}$, where l_r is the length of the

fiber and A_{Kf} is the cross section of the fiber. The work done to dV_K is used to stretch the fibers that are in that volume:

$$\bar{\mathbf{T}}_K \cdot \dot{\bar{\mathbf{F}}} = \sum_{\theta} \sigma_{Kf}^{\theta} f_r^{\theta} \dot{\Lambda}_{\theta} \quad (7)$$

where $\sigma_{Kf}^{\theta} = \frac{F_r^{\theta}}{A_{Kf}}$ is the stress in fiber with orientation θ (reference configuration). The

summation is extended to all the directions in the felt.

But $\bar{\mathbf{T}}_K \cdot \dot{\bar{\mathbf{F}}}$ may be rewritten as:

$$\bar{\bar{T}}_K \cdot \dot{\bar{\bar{F}}} = J \left(\bar{\bar{T}} \cdot \bar{\bar{F}}^{-T} \right) \cdot \dot{\bar{\bar{F}}} = J \bar{\bar{T}} \cdot \dot{\bar{\bar{G}}} = J \bar{\bar{T}} \cdot \left(\frac{\dot{\bar{\bar{G}}} + \dot{\bar{\bar{G}}}^T}{2} \right) = \frac{1}{2} J \bar{\bar{T}} \cdot \left(\bar{\bar{F}}^{-T} \dot{\bar{\bar{F}}}^T + \dot{\bar{\bar{F}}} \bar{\bar{F}}^{-1} \right) \quad (8)$$

$$\bar{\bar{T}}_K \cdot \dot{\bar{\bar{F}}} = \frac{1}{2} J \bar{\bar{T}} \cdot \bar{\bar{F}}^{-T} \left(\dot{\bar{\bar{F}}}^T \bar{\bar{F}} + \bar{\bar{F}}^T \dot{\bar{\bar{F}}} \right) \bar{\bar{F}}^{-1} = \frac{1}{2} J \bar{\bar{T}} \cdot \bar{\bar{F}}^{-T} \dot{\bar{\bar{C}}} \bar{\bar{F}}^{-1} \quad (9)$$

$$\bar{\bar{T}}_K \cdot \dot{\bar{\bar{F}}} = \frac{1}{2} J \bar{\bar{F}}^{-1} \bar{\bar{T}} \bar{\bar{F}}^{-T} \cdot \dot{\bar{\bar{C}}} = \frac{1}{2} J \bar{\bar{T}}_K \cdot \dot{\bar{\bar{C}}} \quad (10)$$

The second kind Piola-Kirchhoff tensor ($\bar{\bar{T}}$) has been introduced in the last equation. On the other hand the work done to the fiber can also be rewritten as:

$$\sum_{\theta} \sigma_{kf}^{\theta} f_f^{\theta} \frac{\dot{\bar{\bar{C}}} \bar{\eta}_{\theta} \cdot \bar{\eta}_{\theta}}{2 \sqrt{\bar{\bar{C}}} \bar{\eta}_{\theta} \cdot \bar{\eta}_{\theta}} = \frac{1}{2} \left[\sum_{\theta} \sigma_{kf}^{\theta} f_f^{\theta} \frac{\bar{\eta}_{\theta} \otimes \bar{\eta}_{\theta}}{\sqrt{\bar{\bar{C}}} \bar{\eta}_{\theta} \cdot \bar{\eta}_{\theta}} \right] \cdot \dot{\bar{\bar{C}}} \quad (11)$$

Since (10) and (11) should be valid for every stress state, i.e. every $\dot{\bar{\bar{C}}}$, it is possible to write:

$$\bar{\bar{T}}_K = \sum_{\theta} \sigma_{kf}^{\theta} f_f^{\theta} \frac{\bar{\eta}_{\theta} \otimes \bar{\eta}_{\theta}}{\sqrt{\bar{\bar{C}}} \bar{\eta}_{\theta} \cdot \bar{\eta}_{\theta}} \quad (12)$$

or, in the limit:

$$\bar{\bar{T}}_K = f_f \int_{\theta} \frac{\sigma_{kf}^{\theta}}{\Lambda(\theta)} \varphi(\theta) \bar{\eta}_{\theta} \otimes \bar{\eta}_{\theta} d\theta \quad (12)$$

Equation (12) relates the stress in the felt with the stress in the fiber through $\varphi(\theta)$, which is the probability density function ($\varphi(\theta) d\theta$ gives the number of fibers that are oriented between θ and $\theta+d\theta$). f_f in that equation is the volumetric fraction of fibers. Equation (12) gives the constitutive equation of the felt once some assumptions are made.

b) Example: Elastic and isotropic felt with small strains

If we assume the fibers are elastic then the stress in the fiber only depends on the instantaneous strain on them, and not on the previous history:

$$\sigma_{Kf} = \sigma_{Kf}(\epsilon) \quad (13)$$

If small strains are assumed the following approximations are true:

$$J \approx 1 ; \bar{F} \approx \bar{I} ; \bar{C} \approx \bar{I} + 2 \bar{\epsilon} ; \sqrt{\bar{C} \bar{\eta}_\theta \cdot \bar{\eta}_\theta} - 1 \approx (\bar{\epsilon} \bar{\eta}_\theta) \cdot \bar{\eta}_\theta \quad (14)$$

If ϵ_I and ϵ_{II} are the principal strains in a point of the felt, and \bar{p}_I and \bar{p}_{II} an orthonormal base in the direction of the principal strains (see Figure 53) then it is possible to write:

$$\bar{\eta}_\theta = \cos \theta \bar{p}_I + \sin \theta \bar{p}_{II} \quad (14)$$

$$\bar{\eta}_\theta \otimes \bar{\eta}_\theta = \cos^2 \theta \bar{p}_I \otimes \bar{p}_I + \sin^2 \theta \bar{p}_{II} \otimes \bar{p}_{II} + \sin \theta \cos \theta \bar{p}_I \otimes \bar{p}_{II} + \sin \theta \cos \theta \bar{p}_{II} \otimes \bar{p}_I \quad (15)$$

and since

$$\bar{\epsilon} = \epsilon_I \bar{p}_I \otimes \bar{p}_I + \epsilon_{II} \bar{p}_{II} \otimes \bar{p}_{II} \quad (16)$$

(assuming only in-plane stresses) then

$$\bar{\epsilon} \bar{\eta}_\theta = \epsilon_I \cos \theta \bar{p}_I + \epsilon_{II} \sin \theta \bar{p}_{II} \quad (17)$$

and the strain of the fiber results in

$$(\bar{\epsilon} \bar{\eta}_\theta) \cdot \bar{\eta}_\theta = \epsilon_I \cos^2 \theta + \epsilon_{II} \sin^2 \theta \quad (18)$$

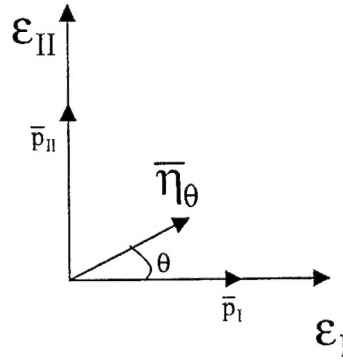


Figure 53: Principal strains orthonormal base

If the fiber is linear elastic then:

$$\sigma((\bar{\epsilon} \bar{\eta}_\theta) \cdot \bar{\eta}_\theta) = E_f (\epsilon_I \cos^2 \theta + \epsilon_{II} \sin^2 \theta) \quad (19)$$

where E_f is the elastic modulus of the fiber.

So for the elastic and small strains case Equation (12) comes to (Piola and Cauchy tensors are the same for small strains):

$$\bar{\bar{T}} = \bar{\bar{T}}_K = \int_{\theta} \frac{\sigma_{kf}^{\theta}}{\Lambda(\theta)} \varphi(\theta) \bar{n}_{\theta} \otimes \bar{n}_{\theta} d\theta = f_f \int_{\theta} \sigma((\bar{\bar{\epsilon}} \bar{n}_{\theta}) \cdot \bar{n}_{\theta}) \varphi(\theta) \bar{n}_{\theta} \otimes \bar{n}_{\theta} d\theta \quad \text{or}$$

$$\bar{\bar{T}} = f_f \int_{\theta} E_f (\epsilon_1 \cos^2 \theta + \epsilon_{11} \sin^2 \theta) \varphi(\theta) (\cos^2 \theta \bar{p}_1 \otimes \bar{p}_1 + \sin^2 \theta \bar{p}_{11} \otimes \bar{p}_{11} + \sin \theta \cos \theta \bar{p}_1 \otimes \bar{p}_{11} + \sin \theta \cos \theta \bar{p}_{11} \otimes \bar{p}_1) d\theta \quad (20)$$

For clarity we can rewrite (20) in matrix form ($\varphi(\theta) = 1/\pi$ if isotropic):

$$\begin{bmatrix} \sigma_1 \\ \sigma_{11} \end{bmatrix} = \frac{f_f E_f}{\pi} \begin{bmatrix} A_{11} & A_{12} \\ A_{12} & A_{22} \end{bmatrix} \begin{bmatrix} \epsilon_1 \\ \epsilon_{11} \end{bmatrix} \quad (21)$$

where

$$A_{11} = \int_{-\pi/2}^{\pi/2} \cos^4 \theta d\theta; A_{22} = \int_{-\pi/2}^{\pi/2} \sin^4 \theta d\theta; A_{12} = \int_{-\pi/2}^{\pi/2} \cos^2 \theta \sin^2 \theta d\theta$$

Equations (12) and (20) show the complexity of finding a constitutive equation for the felt. This simplified model assumes no slipping between the fibers, but still gets extremely complicated if small strains cannot be assumed. We also know that the felt is not isotropic but orthotropic. Let's write the constitutive equation for a linear non-isotropic felt.

c) Example: Elastic and orthotropic felt with small strains

Beginning with Equation (12) we can write

$$\bar{\bar{T}} = f_f \int_{\theta} E_f (\bar{\bar{\epsilon}} \bar{n}_{\theta} \cdot \bar{n}_{\theta}) \varphi(\theta) \bar{n}_{\theta} \otimes \bar{n}_{\theta} d\theta \quad (23)$$

If we assume a distribution of fibers like, for example, a cosine from an arbitrary direction \bar{N} :

$$\varphi(\theta) = \frac{1}{\pi} + B \cos(2\theta) \quad (24)$$

And we can write, being \bar{N} and \bar{M} the orthonormal base:

$$\bar{n}_{\theta} = \cos \theta \bar{N} + \sin \theta \bar{M} \quad (25)$$

$$\bar{\bar{\epsilon}} = \epsilon_{11} \bar{N} \otimes \bar{N} + \epsilon_{22} \bar{M} \otimes \bar{M} + \epsilon_{12} (\bar{M} \otimes \bar{N} + \bar{M} \otimes \bar{N}) \quad (26)$$

Using (24)-(26) Equation (23) can again be written in a matrix form:

$$\begin{bmatrix} \sigma_{11} \\ \sigma_{22} \\ \sigma_{12} \end{bmatrix} = f_f \begin{bmatrix} 3 + 4\phi_1 + \phi_2 & 1 - \phi_2 & 0 \\ 1 - \phi_2 & 3 - 4\phi_1 + \phi_2 & 0 \\ 0 & 0 & 1 - \phi_2 \end{bmatrix} \quad (27)$$

Where $\phi_i = \int_{-\pi/2}^{\pi/2} \phi(\theta) \cos(2i\theta) d\theta$

It is remarkable to see in (27) that only two parameters allow to describe a general orthotropic material made of fibers.

4.3 Summary

A constitutive equation was developed with the help of continuum mechanics. The constitutive equation is for materials made of an arbitrary distribution of fibers, but with the serious limit of linearity and small strains. Unfortunately Fraglight strains and deflections are very large, up to 100%, so the small strains assumption would not catch its real behavior. Trying to rewrite (12) without the assumptions of small strains would be a much more difficult job.

REFERENCES

- 1 Philip M. Cunniff, A Semiempirical Model for the Ballistic Impact Performance of Textile-Based Personnel Armor, *Textile Res. Journal*, **66** (1), 45-59, 1996
- 2 Vinson and Zukas, On the Ballistic Impact of Textile Body Armor, *Journal of Applied Mechanics*, 263-268, 1975
- 3 James D. Walker, Constitutive Model for Fabrics With Explicit Static Solution and Ballistic Limit, *18th International Symposium on Ballistics*, San Antonio, TX, 1999
- 4 S. Chocron, A Simple Analytical Model to Simulate Textile Fabric Ballistic Impact Behavior, *Textile Res. Journal*, **67** (7), July 1997
- 5 Philip M. Cunniff, An Analysis of the System Effects in Woven Fabrics Under Ballistic Impact, *Textile Res. Journal*, **62** (9), 495-509, 1992
- 6 Gerhard A. Holzapfel, *Nonlinear Solid Mechanics*, John Wiley & Sons, 2000